

Chapter 8

Electromagnetic Nanowire Resonances for Field-Enhanced Spectroscopy

Annemarie Pucci, Frank Neubrech, Javier Aizpurua, Thomas Cornelius,
and Marc Lamy de la Chapelle

Abstract Electromagnetic resonances of metal nanowires lead to strong enhancement of the near field of the particle. Antenna-like resonances that give the biggest enhancement are explained theoretically. The preparation of high-quality wires is introduced. Spectroscopic results for resonance curves are shown and discussed with respect to field enhancement. Surface-enhanced Raman scattering and surface-enhanced infrared absorption are introduced focusing on nanowire-assisted configurations, and examples of these enhanced spectroscopies for molecules on resonant nanowires are shown.

8.1 Introduction

Nanosized metal objects exhibit interesting optical properties with numerous applications in technology and life science [1–4]. They may be used as effective hosts for spectroscopy and light emission [5–8, 118]. The optical properties of such metal nanoobjects are dominated by electromagnetic resonances that are related to considerable electromagnetic field enhancement in the proximity of a nanoparticle [9]. If such resonances are due to free-charge carrier (plasmon-like) excitations, this field enhancement can be particularly strong, which is related to the large negative real part of the dielectric function in a metal (for energies below the plasma edge), much larger than characteristic values of other excitations, like for example optical phonons in a halide or oxide. The fields are strongly enhanced in the range of few nanometers from sharpened metal points, if the radius of curvature is much smaller than the incident illumination wavelength. Therefore rod-like metallic particles may give higher nearfield strength than spherical ones, as we will show below. The dimensions of the particle are of multifold importance for resonance positions and the related field enhancement. For example, in case of a prolate ellipsoid, two fundamental dipole-like resonances exist. The excitation with electric field along the long axis is shifted towards lower frequencies as the ellipsoid aspect ratio increases. When the wavelength is comparable to the length of the particle, retardation

is triggered and the limited velocity of light has to be considered in the calculations of resonance effects. Such particle excitations are known as antenna resonances. On the other hand, resonances of spherical nanoparticles are known as Mie resonances [10] and can be calculated in the electrostatic limit. An ideal metal antenna with a length several orders of magnitude larger than the diameter and with negligible penetration depth (skin depth) of the electromagnetic field into the antenna compared with the diameter has its fundamental antenna resonance wavelength at about two-times the length. This relationship is a rough estimate also for nanoantennas (with a deviation up to about 30% from the exact resonance position). It means that resonances in the infrared need lengths of a few to several microns. Such antennas can be fabricated as wires with diameters down to a few ten nanometers, i.e. considerably smaller than the wavelength, which enables high field enhancement at the wire ends. To get resonances in the visible range, one can use shorter wires or higher order antenna excitations. In both cases field enhancement is smaller than in the infrared.

The resonant nearfield enhancement can be increased by the interaction with another resonant particle in proximity. For example, an extremely high optical nearfield enhancement localized in nanoslits between gold nanorods is possible to obtain [11]. This example indicates that the surface plasmon resonances of metal nanoparticles can be exploited to confine electromagnetic radiation to a volume of subwavelength dimensions [12]. This volume can also be a nanohole in a continuous metal film and the plasmon resonances of that structure give rise to the phenomenon of enhanced transmittance through apertures smaller than the incident wavelength [13].

In periodic metallic structures the electromagnetic coupling to neighbor particles or holes, respectively, influences the resonance conditions. These photonic (plasmonic) effects and the enhanced transmittance have motivated a renewed interest in particle scattering studies, with the aim of understanding the nearfield coupling of closely spaced metallic particles much smaller than the optical wavelength [14]. Because of that coupling, the lattice structure and the lattice constants determine the conditions for wavevector and frequency of transmittance and of reflectance maxima, i.e. a band structure for photons arises [15].

The spectral properties of such photonic structures are influenced by the real dynamic conductivity of the metal that may be different to the textbook value if a lot of defects from preparation may shorten the mean free path of free charge carriers. In case of dimensions of only several nanometers surface scattering of free charge carriers limits that mean free path [16]. From the mid-infrared to the visible range the shortened mean free path of free charge carriers affects only very weakly the skin depth, but the real part of the conductivity is changed.

The substrate of a metal nanostructure is of relevance for three reasons: It may chemically interact with the metal modifying the surface properties at the interface, charge carriers may penetrate through the interface, and the electromagnetic field is changed because of the polarizability of the substrate. Thus, the substrate surface structure and chemical surface composition are crucial.

A metal-island film can be considered as a more or less random array of metal nanoparticles with distribution of sizes, shapes, and orientations. Optical spectra for

electric field parallel to the layer show a broad resonance that further broadens toward lower frequency with decreasing particle distances. At the percolation threshold, where at least one conductive cluster has formed because of coalescence of particles, the optical spectra (transmittance, reflectance, absorbance) are nearly frequency independent [17]. On a local scale, strong field enhancement is predicted for such films, especially at certain “hot spots” for random (fractal-structured) metal-island film; an effect that is used to explain extraordinary strong surface enhanced Raman scattering (SERS), different to ordered metal structures [18–20]. The basic idea is that the local field enhancement obtained by metal nanostructures at resonance produces increased local response of an excitation at the resonance frequency. This excitation can be of vibrational nature (SEIRA = surface enhanced infrared absorption), of electronic nature (second harmonic generation A. Bouhelier, M. Beversluis, A. Hartschuh, and L. Novotny (2003) Near-Field Second-Harmonic Generation Induced by Local Field Enhancement. *Phys Rev Lett* 90: 013903-1), and a combination of both (SERS, fluorescence [5, 119]).

Microscopy techniques based on IR absorption and Raman scattering would be ideally suited for label-free imaging of molecular complexes in life sciences (DNA, proteins, etc.). Because of the sharp and well-defined spectral signatures of the molecules, in fact, no sample’s labeling would be needed. These two techniques are already well known as powerful tools to characterize organic materials since the vibrational modes are actual fingerprints of the studied species (information on the molecule conformation, on chemical groups, and bonding etc.). The two vibration spectroscopies are complementary with respect to their application possibilities and to the excitation cross-sections of molecular vibrations. Moreover, the Raman spectrum may be difficult to observe and even hidden because of strong fluorescence emission especially for biological species; however, the spatial resolution achieved can be less than 1 μm and can then allow a very precise characterization. Concerning IR spectroscopy, there is no fluorescence, but the spatial resolution is much larger (around 10 μm). Unfortunately, IR absorption and Raman scattering cross-sections are far too low (10^{-20} – 10^{-30} cm^2) for fast imaging applications and suffer from their poor spatial resolution.

But SERS and SEIRA have indicated the pathway towards the extreme amplification of the electromagnetic field on the local scale, required to accomplish nanoscale resolved imaging, and single-molecule sensitivity. They have the power to get nanoscale information on specific molecular groups and on their response behavior to external disturbances without artificial labeling. Sufficiently high and predictable nearfield enhancement can be achieved with antenna-like plasmon resonances of rod-like metal particles (here they are called “wires”). Until now, surface enhanced scattering studies that approached single-molecule sensitivity have used randomly distributed metal particles, which yields only qualitative information. It is a great challenge to produce well-defined antenna structures according to precise theoretical predictions for maximum field enhancement over the whole frequency range of the molecular excitations of interest.

In this chapter on electromagnetic nanowire resonances only metal particles are considered. First, the resonances are explained theoretically as ideal antennas and

within full electrodynamics. It follows two examples on wire fabrication including physical characterization; however there are other means to obtain metallic nanowires. In the later sections, examples for optical spectroscopy of wires in different spectral regions are introduced. The last two sections are devoted to examples from surface enhanced spectroscopy.

8.2 Theory of Nanowire Resonances and Simulation of Spectra

In this section we review some of the main factors governing the optical response of metallic nanowires: directionality, surrounding medium, and coupling. The theoretical input of their optical response is a key element for understanding, producing, engineering, and obtaining appropriate hosts for optimal response in field-enhanced spectroscopies.

8.2.1 Basics of Nanowire Resonances: Surface Plasmons and Ideal Antennas

If metal structures are exposed to electromagnetic radiation, modes of collective charge carrier motion, called plasmons, can be excited. Many properties of such plasmons can be qualitatively understood in the semiclassical model as follows.

In the range of the skin depth the incident electric field shifts the free electrons collectively with respect to the positive charge of the fixed lattice ions. A charge carrier separation is built up. The attraction between the separated charges produces a restoring force that mainly depends on the dynamic polarizability of the metal in the intraband region, like plasma frequency and relaxation rate [21].

This force gives rise to collective electronic oscillations at the surface of the metal, known as surface plasmon [22]. The surface plasmons can propagate along a distance of several tens of micrometers on the surface of a film and the plasmon resonance condition is achieved for one specific wavevector and one specific excitation wavelength. In the case of one nanoparticle, the surface plasmon is confined to the three dimensions of the nanostructure and it is then called localized surface plasmon (LSP) [22,23]. In this situation, the LSP resonance depends on the metallic nature (effect of the metal permittivity) and on the geometry (effect of the confinement of the electron cloud) of the nanostructure. The strength of the oscillation is influenced from radiative (scattering) and nonradiative (absorption) damping. Excitations with resonance frequencies in the visible or near ultraviolet spectral range are investigated experimentally [2] and theoretically by solving Maxwell's equations within the quasistatic limit [10] if particle dimension are much smaller than the wavelength (Mie resonances).

It has been shown through the quasistatic approximation that the LSP resonance, for a nanoparticle in air, is achieved when the excitation wavelength corresponds to the one determined by the following condition: $\text{Re}(\epsilon) = 1 - 1/Q_{\text{eff}}$ where ϵ is the

metal dielectric function and Q_{eff} is the effective depolarization factor described in [23]. This factor takes into account the shape of the particle. However, Q_{eff} can also include some first order corrections to the quasistatic model such as the dynamic depolarization or the radiation damping.

For a sphere, $Q_{\text{eff}} = 1/3$, and thus the resonance condition will be $\text{Re}(\epsilon) = -2$, which is fulfilled at 484 nm for gold, at 354 nm for silver, and at 367 nm for copper [24]. The experimental values are different not only because of the effect of interband transitions on the plasmon resonance but also because of deviations from the spherical shape. For a nanoparticle with different shape, Q_{eff} is lower than 1/3 and can be very small. In this case, the LSP resonance position is redshifted. The value of Q_{eff} is closely related to the detailed shape of the nanoparticle. Going from spherical particles to elongated ones, the plasmon resonance has split into different branches according to the electric field direction and the geometry dependence becomes increasingly important, in particular for the LSP resonance [2]. The low-energy LSP resonance can be detected even in the mid-IR for an adequate length of the nanoparticle [25]. The larger is the aspect ratio (long axis L /small axis D) of the particle the lower the frequency of this mode (for constant D). If the wire length approaches the range of the exciting wavelength, the effects of retardation dominate the resonance condition and the limited speed of light results in a direct dependence of the resonance frequency on the absolute dimensions of the particle. This is well known from purely classical theory of scattering of electromagnetic waves by metal objects [26]. If the smallest dimension of the particle is much larger than the skin depth of the electromagnetic radiation in the metal, also real metal wires can be estimated as perfect conductors. For ideal metal objects it is assumed that the light does not penetrate into the particle. This means an infinitely large negative dielectric function. Then, antenna-like resonances occur if the length L of an infinitely thin wire matches with multiples of the wavelength λ , i.e.

$$L = \frac{\lambda}{2n} \cdot l, \quad (8.1)$$

where l is a natural number and n is the refractive index of the surrounding medium. The fundamental mode of the resonance corresponds to $l = 1$, higher dipole-like excitations correspond to odd l . These higher orders of resonance can be observed as new bands on the extinction spectra at wavelengths lower than the dipolar resonance.

Electromagnetic scattering of perfect conducting antennas with D smaller than the wavelength and L in the range of the wavelength is discussed in classical antenna scattering theory. These scattering calculations point out an influence of a nonnegligible diameter D in comparison with the wavelength on the resonance frequency and line shape [27]. Considering nanowires with the same length L , but different diameters D , one finds out that the smaller the aspect ratio L/D , the more broadened the resonance and the lower the resonance wavelength.

It is a frequently used approximation to consider a metal nanowire as an ideal antenna. This approach has been proposed also for the modeling of nanowires in the visible spectral range, as described for example by Martin et al. [28]. The authors of this work assume the nanowire as a perfect conductor, show the existence of antenna modes by means of the finite difference element in time domain (FDTD), and

demonstrate that the field is enhanced at the tip of the nanowire when the excitation wavelength corresponds to an antenna mode.

The assumption of having a perfect conductor means that $-\text{Re}(\epsilon)$ is either infinite or at least very large. This is not valid in the visible range. That approximation is applicable for very large wavelengths only, i.e. from the far infrared up to radio frequencies. From the mid-IR and to UV range, the details of the dielectric function of the nanowire-material (including surface induced effects) should be taken into account because they determine the excitations of the free electron gas in the wire.

In addition to the mentioned effects, the polarizability of the surrounding media affects the optical properties of metal nanoparticles. Regarding the effect of the substrate (with the refractive index $n_s = \sqrt{\epsilon_s}$) on which the nanowires are placed and the surrounding medium (air, refractive index of 1), an effective medium completely embedding the wires is a reasonable assumption. Its effective dielectric constant is given by the following equation [27]:

$$\epsilon_{\text{eff}} = \frac{1}{2}(1 + \epsilon_s) \quad (8.2)$$

Using the relation $n = n_{\text{eff}} = \sqrt{\epsilon_{\text{eff}}}$ the influence of the substrate on optical spectra can be described well [29].

8.2.2 Factors Governing Nanowire Plasmon Modes

Electromagnetic resonances of nanowires in the optical and near infrared are a result of several effects. On the one hand, as pointed out in the previous section, the structure of a finite one-dimensional conductor supports efficient antenna behavior for certain wire lengths. On the other hand, the end of the nanowires in a relatively sharp and abrupt surface is a perfect candidate to host a lightning rod effect. Finally, the valence electrons in metals oscillating freely and coherently on the wires surface as a response to radiation produces certain resonant modes, known as surface plasmons, that determine the optical and near infrared response of these structures. The solution of Maxwell's equations for metallic nanorods with the consideration of the exact length and width of the wire and the use of a local dielectric response to characterize the optical response of the metal is able to account for all those effects. One of the main features in the optical response of metallic nanorods is connected with the strong directionality of the plasmon response. The presence of one dimension much longer than the other two generates a long wavelength resonance (the low-energy LSP), also called longitudinal plasmon, which presents a much lower energy than the low wavelength resonances also called transversal plasmon [30]. In Fig. 8.1a we show the calculated optical extinction spectra of a 500 nm long gold nanorod with two different diameters, 80 and 200 nm, respectively. The excitations for two different polarizations (parallel and perpendicular to the long wire axis) of the incoming light are completely different not only in resonance wavelength but also in extinction at resonance. The long wavelength peak is associated with the

dipolar-like polarization of the long axis, whereas the short wavelength peak is associated with transversal polarizations at the nanorod. The strength of the latter is noticeably smaller as the induced charge at the surfaces is scattered along the rod walls. For the longitudinal excitation, the induced charge is piled up at the rod ends, driving a considerable strength of the induced dipole. In Fig. 8.1a an extinction spectrum for the thinner wire as an ideal antenna ($L/D \gg 1$, perfect conducting metal, calculation according to [26]) is shown for comparison.

In optical and infrared spectroscopy usually only the antenna-like surface modes are identified, but higher order modes are also solutions supported by the geometry and identified for different applications as in SERS [31]. For a given external excitation, the total surface induced charge σ can be expressed as a weighted summation of the surface modes: $\sigma = \sum_{lm} A_{lm} \sigma_m^l e^{im\varphi}$, where σ_m^l is the induced surface charge density of the l mode, projected over the azimuthal index m , and A_{lm} is the weight of the σ_m^l mode, which depends on the characteristics of the incoming radiation (polarization, intensity, angle of incidence, etc.) on the geometry, and on the material. In Fig. 8.1b we show the polarization patterns for the first $m = 0$ and $m = 1$ modes. The set of surface modes σ_m^l spread out as antisymmetric A (net dipole) and symmetric S solutions (no net dipole), all over the spectrum, from the lowest energy mode (σ_0^0) up to modes with energies close to the planar surface plasma frequency $\omega_s = \omega_p / \sqrt{2}$ for free charge carriers with the bulk plasma frequency ω_p . The first antisymmetric mode (σ_0^1) is the lowest energy physical mode and shows total net dipole. This mode is effectively excited by light linearly polarized along the rod axis, giving rise to the longitudinal plasmon. Higher order modes are also present in the spectrum for higher energies, and although they are usually masked in optical spectra because of pile up, homogeneous broadening, and lower excitation weight, they have been identified for example in photoluminescence [32–34] and SERS [31]. On the other hand, the first mode with $m = 1$ (σ_1^1) is usually associated with the transverse peak of extinction. This mode presents cosine dependence around the azimuthal angle of the rod, therefore is effectively excited by light linearly polarized perpendicular to the rod axis.

A similar behavior can be found for metallic wires larger than several hundred nanometers. The increasing size of the nanoantennas makes the resonances to appear at wavelengths that present larger negative values of the dielectric function, i.e. for wavelengths well in the mid infrared portion of the spectrum in the case of micron-sized wires. It is actually this extension of the resonant behavior to micron-sized antennas what makes these structures optimal candidates for surface enhanced Raman spectroscopy (SERS) and surface-enhanced infrared absorption spectroscopy (SEIRA).

Tuning of the optical response can be achieved via changing the length and adjusting the width of the nanorod. Several detailed geometries have been used to calculate the scattering effects of nanorods and nanowires. One of the most commonly used has been the ellipsoidal geometry since it presents analytical solutions for the polarizabilities in an electrostatic approximation [35, 36]. As the nanorods become larger in size, the shape of the wires departs from an ellipsoid, therefore a geometry with straight walls and hemispherical ends seems to be reasonable to

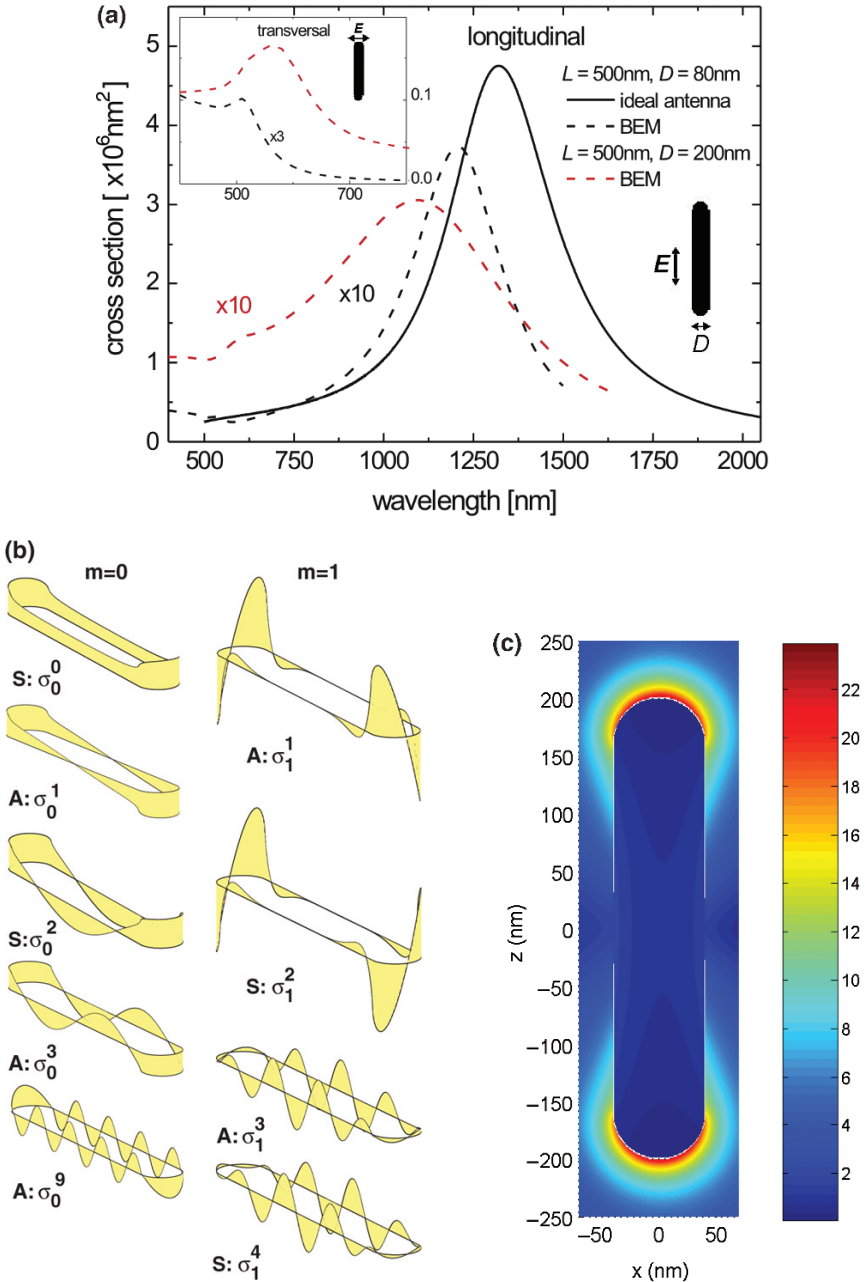


Fig. 8.1 (a) Extinction cross-section (in the farfield) of 500 nm long gold nanorods for different polarizations of the incoming light calculated with BEM and with classical theory for ideal antennas. Longitudinal and transverse (inset) plasmon excitations can be observed. (b) Surface charge oscillation patterns σ_m^l of modes in a nanorod. First order modes for $m = 0$ and $m = 1$ symmetry as calculated from solving Laplace's equation. (c) Distribution of nearfield enhancement for the fundamental antenna resonance (at 1255 nm) of a gold nanorod with $L = 400 \text{nm}$ and $D = 80 \text{nm}$ at (BEM result, field-enhancement factor according to the different colours as defined on the right)

describe the wires. Moreover, effects of retardation have a strong influence, reducing the energy of the plasmon resonances. Especially for the case of micron-sized antennas, where the interactions along the edges and the walls can be comparable to the incoming wavelength, full electro-dynamical calculations are needed to account for the position of the resonances. Several techniques have been developed to solve Maxwell's equations in inhomogeneous media. All of them present advantages in certain aspects and disadvantages in others. For example, the dipole discrete dipole approximation (DDA) [37], finite difference methods in time domain (FDTD) [38], multiple multipole expansion (MMP) techniques [39], transfer matrix methods [40], or finite element methods in frequency domain, are among some of the most commonly used techniques to solve Maxwell's equations. Here we explain and apply the boundary element method (BEM) [41,42], where the surfaces separating two different media are discretized, and Maxwell's equations are expressed in integral form, in terms of the scalar potential ϕ and the vector potential \mathbf{A} , involving the surface charge densities σ_j and the currents \mathbf{h}_j at the boundaries separating two different media:

$$\phi(\mathbf{r}) = \phi^e(\mathbf{r}) + \int_{S_j} d\mathbf{s} G_j(|\mathbf{r}-\mathbf{s}|) \sigma_j(\mathbf{s}) \quad (8.3)$$

and

$$\mathbf{A}(\mathbf{r}) = \mathbf{A}^e(\mathbf{r}) + \int_{S_j} d\mathbf{s} G_j(|\mathbf{r}-\mathbf{s}|) \mathbf{h}_j(\mathbf{s}) \quad (8.4)$$

with

$$G_j(|\mathbf{r}-\mathbf{s}|) = \frac{e^{ik_j|\mathbf{r}-\mathbf{s}|}}{|\mathbf{r}-\mathbf{s}|} \quad (8.5)$$

the scalar-wave Green's function propagator in medium j , and $\mathbf{k}_j(k_j = (\omega/c)\sqrt{\epsilon_j})$ is the wave vector of light in medium j . $\phi^e(\mathbf{r})$ and $\mathbf{A}^e(\mathbf{r})$ are the potentials created by the external source. Each medium is characterized by its local dielectric function $\epsilon(\omega)$, which represents the local bulk dielectric response. Solving the integral equations in (8.3) and (8.4), involving the self-consistent induced charges and currents, allows for obtaining the near field and far field distribution from any scattering object [11,43]. We will describe the geometry of the rods as a cylindrical wire of total length L , with hemispherical ends of radius R that relate to the width of the rod D as $D = 2R$. This geometry seems to account very accurately for all the experimental features in the optical scattering of nanorods [11]. Figure 8.1c shows the nearfield enhancement for such nanorod at the fundamental antenna resonance.

In Fig. 8.2a we present the extinction cross-sections of different gold nanoantennas and microantennas for incoming light polarized along the long axis. The extinction peaks spread all over from the optical to the mid-infrared range of the spectrum as a function of rod length. As the rod becomes longer, the spectral peak is red shifted. As we show in Fig. 8.2b, the evolution of the resonances (extinction peaks) presents a quasilinear behavior that is described by the relationship $L \approx \lambda/2.5$ for such relatively wide wires. This behavior departs from the standard $L = \lambda/2$ for ideal antennas. As the length of the rods exceeds $5\mu\text{m}$, the slope of the resonances

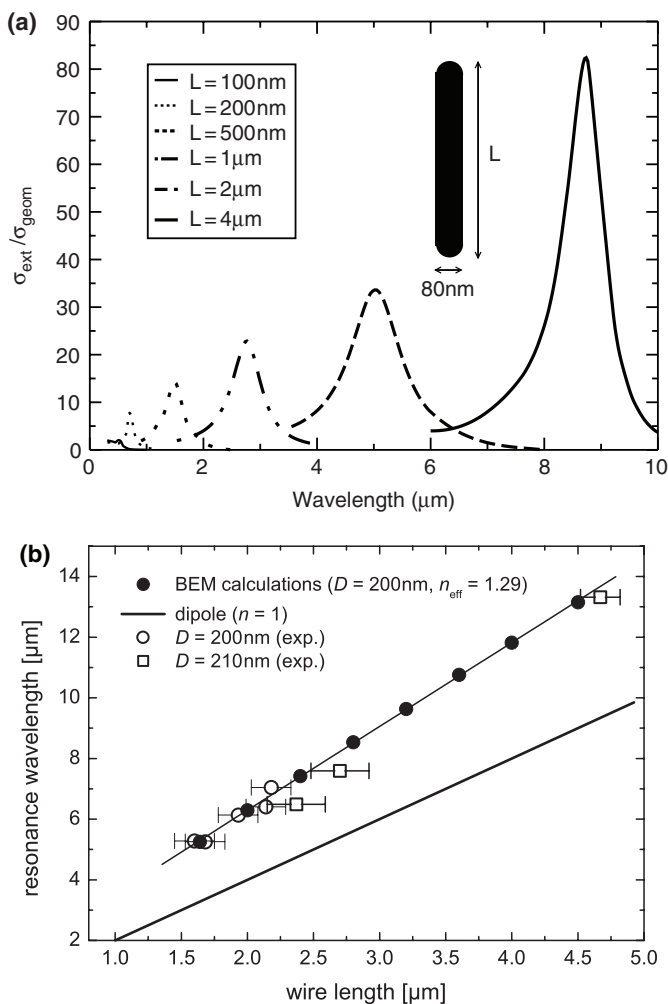


Fig. 8.2 (a) Total extinction cross-section of 80 nm wide gold nanowires for different lengths L in the farfield. (b) Linear behavior of resonances with wire length for different diameters. A deviation from antenna theory is observed in the resonances position, see curves for dipole (ideal antenna). The polarizability of the substrate is considered with the effective refractive index n_{eff} . The substrate for the experiments was KBr

is reduced to $L \approx \lambda/2.2$, therefore approaching slowly to the behavior of a perfect conductor. When the skin depth to diameter ratio is very large, the denominator is enhanced up to even 10.

As shown in Fig. 8.2a, the extinction cross-section of an elongated wire normalized to its geometrical surface is at least one order of magnitude larger than the corresponding normalized extinction in a spherical particle. The finite conductivity (finite negative dielectric function) of the metals in this range of the spectrum is responsible for the modification of the slope. It is commonly assumed in the

literature that this linear behavior follows a scaling law for the aspect ratio in different rods. Even though that is the case in a nonretarded solution of electrical fields, this is not the case when the full electromagnetic solution to the scattering problem is considered. Because of retardation, a set of rods with a certain width follows a linear behavior that is different to the linear behavior of another rod with a different width [44]. This effect is more evident for very thin wires.

Surface plasmon modes are mainly given by the plasma frequency of the electron gas that adapts to the geometrical boundaries of the system, generating the surface plasmons. Both gold and silver are commonly used for nanoparticle plasmonics because of the relatively easy production and manipulation. Their optical responses do not correspond exactly to that of a free electron gas, due to the role of d electrons, but a modified Drude-like function describes well their responses in a wide range of the spectrum. For optical frequencies, gold and silver show distinctively different surface plasmon resonances. However, in the near and mid infrared portions of the spectrum, both materials adopt large negative values of the permittivity, giving rise to similar positions and weight of the antenna resonances. Another metal that behaves as a free electron gas and is well described by a Drude response function is aluminum. Plasmon resonances in this material fall into the ultraviolet ($\lambda_s = 110\text{nm}$), but its nanorod resonances can fall in the optical portion of the spectrum because of the induced redshift. Another set of interesting materials for resonant response in the infrared are polar materials such as SiC [45]. In this case, the phonon-polaritons rather than electrons are responsible for the electromagnetic resonances. Finally, nanorods of semiconductor materials [46] are also another set of materials that can produce electromagnetic resonances in the low frequency region because of the reduced electronic density [47]. We focus in this chapter on pure metallic nanowire resonances.

Earlier we have pointed out shortly how the effect of the surrounding medium needs to be considered for the exact position of the antenna resonance. The medium surrounding a metal nanostructure determines, through its polarizability, how intensely the surface charge density can be induced, and ultimately, which energy the resonance falls into. During the last years, a renewed interest to study the influence of the environment in surface plasmons has occurred because of the capacity of the surface plasmon resonance for sensing the local refractive-index change by monitoring the wavelength shift [48–50]. When dealing with nanowire resonances, and due to the different substrates and media surrounding the wires, it is relevant to establish how strongly the environment affects the optical and near infrared response of the nanorods. As pointed out earlier, an effective medium surrounding the nanowire can account for the main features of the substrate effect. In Fig. 8.3, we show the extinction cross-section of a nanorod when it is surrounded by media with different dielectric constant value. As we increase the permittivity of the surrounding material, the plasmon resonances red-shift. This shifts can be as large as 2000 nm in wavelength for changes of $\epsilon = 1$ to $\epsilon = 3$. An accurate estimation of the effect of the surrounding medium is therefore crucial for the exact description of the resonances position. We typically consider an effective medium given by eq. 8.2, which turns to describe very accurately the substrate effect [29].

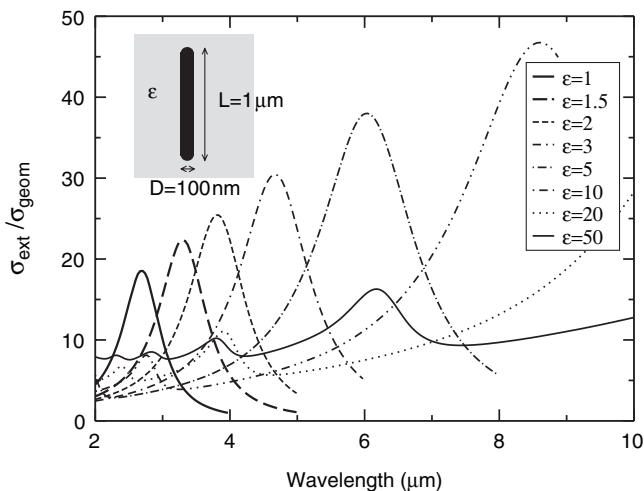


Fig. 8.3 Extinction cross-section (in the farfield) of a $1\mu\text{m}$ long and 100nm wide gold nanorod in different surrounding media characterized by a dielectric constant ϵ . Large values of ϵ red-shift the longitudinal excitation response towards the infrared

Standard theory of nanorod resonances, on the basis of an electrostatic approach, predicts a scaling law with the rods aspect ratio for the resonances position [30]. It has been mentioned here (in Fig. 8.2b) that this scaling is not fulfilled when an exact full electrodynamical description of the scattering is considered. The width and the length of the rods account separately for the resonances positions, and even though a linear behavior with length is observed and corrected with respect to classical antenna theory, the actual proportionality of the wire length and resonances position is different for different widths.

Coupled metallic systems are known to produce red shifts and plasmon hybridization [51, 52]. The lowest energy resonance usually generates a strong local field in the vicinity of the coupling area. Situations where the coupling produces large field enhancement have been proven to be the key to obtain single molecule sensitivity in SERS [53, 54]. The use of cavities or other effective configurations that produce this large field enhancement has allowed for pushing the limits of this spectroscopy [55], even though certain limits (10^{11}) are inherent to the electromagnetic contribution of the SERS enhancement [20]. Several situations creating large field enhancement and singular optical response have been studied in dimers [56], bowtie antennas [57], and sets of metal nanoparticles [58]. Coupled nanorods have also been treated recently as convenient field-enhancers at the cavity between rods [12, 59, 60].

In an attempt to search for an optimal field-enhancing structure, we present here the results for the optical response when two nanorods are coupled together. A computational study of such a situation has been reported previously [11], and similar effects as those reported in the coupling of dimers have been found. As a general trend, field enhancement increases as the rods are located closer together.

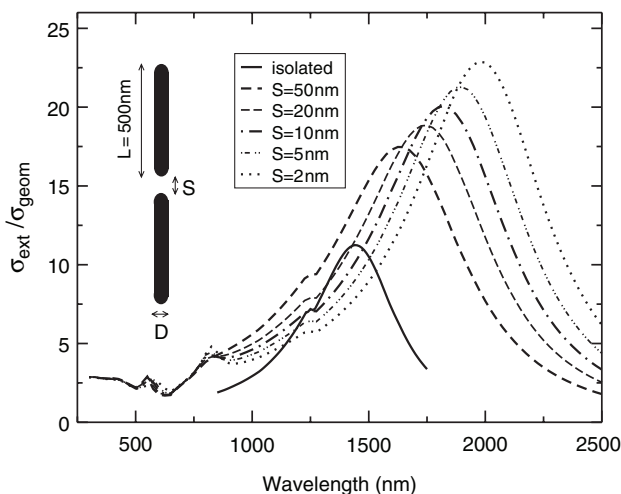


Fig. 8.4 Extinction cross-section of a pair of 500 nm long nanorods for different inter-rod separation distance S , farfield result

The geometry of the rod, with one privileged dimension, is the main effect to consider in the coupling of nanorods. In Fig. 8.4 we plot the extinction cross-section normalized to the geometrical surface for a pair of nanorods with different separation distances. Even though the main effect is obtained in the near field at the cavity, also in the far field, the effects of the coupling are relevant with large shifts into the near IR and larger excitation of the cavity modes for small separation. These effects might increase even more the efficiency of the antennas used for SEIRA, when the samples under study are located at the cavity.

8.3 Nanowire Fabrication

There are many different approaches for metal–nanowire fabrication. Here we introduce only two methods: wire growth in ion tracks of membranes, which is rather exotic, but produces nearly ideally cylindrical wires, and electron-beam lithography, which is a common method today, but the obtained structures do not show cylindrical symmetry. Instead they have a certain height and their two-dimensional shape is fixed by writing with the electron beam.

8.3.1 Wire Growth in Ion Tracks of Membranes

Metal (Au, Cu) [61–65] and semimetal (Bi) [66,67] nanowires were prepared by the template method being schematically depicted in Fig. 8.5. For this purpose, poly-

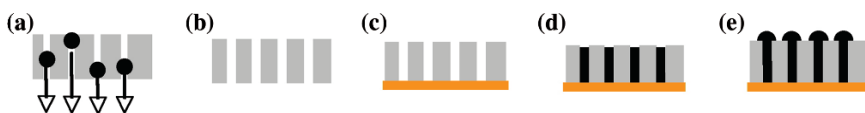


Fig. 8.5 Schema of the template method: (a) A polymer foil is irradiated with swift heavy ions and (b) subsequently etched in aqueous NaOH leading to a nanoporous template. (c) One side is coated with a conductive layer. (d) Metal is deposited electrochemically into the pores. (e) As soon as the metal reaches the opposite side of the membrane, caps start to form on top of the wires

carbonate membranes of thickness $30\ \mu\text{m}$ were irradiated with swift heavy ions that were accelerated to a specific kinetic energy of $11.4\ \text{MeV}$ per nucleon at the UNILAC linear accelerator of GSI (Fig. 8.5a). The applied fluence was varied from a single ion per foil to 10^9 ions per cm^2 . The ions modify the polymer along their trajectories so that cylindrical volumes—so-called latent tracks—are created, which behave chemically different than the nonirradiated polymer. Therefore, the tracks can be selectively dissolved, leading to nanoporous templates (Fig. 8.5b). Prior to chemical etching in $6\ \text{M}$ aqueous sodium hydroxide at 50°C , the foils were exposed to UV light in order to sensitize them for the etchant. The pore diameter is directly proportional to the etching time, i.e., the resulting wire diameter was controlled via the etching process. After rinsing the templates, a thin gold layer was sputtered on one side of the membrane and reinforced by an electrochemically deposited copper layer (Fig. 8.5c). This conductive layer served as cathode during the subsequent electrochemical deposition of the metal in the nanopores (Fig. 8.5d). The electrodepositions were performed in a two-compartment electrochemical cell. When the metal reaches the opposite side of the membrane, caps start to grow on top of the wires (Fig. 8.5e). To fabricate wires of a certain length, the deposition process was interrupted as soon as the wire height reached the desired value, calculated from the charge deposited using Faraday's law.

The depositions were accomplished in a two-compartment electrolytical cell schematically depicted in Fig. 8.6a. For the fabrication of copper and gold nanowires, a simple-salt electrolyte containing $238\ \text{g/l}$ $\text{CuSO}_4 \cdot 5\text{H}_2\text{O}$ and $21\ \text{g/l}$ sulfuric acid and an alkaline cyanide solution, namely potassium dicyanoaurate (I) Puramet 402 bath (Doduco, gold content = $10\ \text{g/l}$) was employed, respectively [61, 62, 64, 65]. As anodes a copper and a gold rod were used during the fabrication process. In Fig. 8.6b, the current versus deposition time is displayed for the fabrication of Cu nanowires with diameter $d = 50\ \text{nm}$ at 50°C and $-120\ \text{mV}$. The deposition curve is dividable in four different sections: (i) The peak in the beginning is due to the electrical double layer which discharges with increasing time. (ii) During the deposition of the metal inside the pores a constant current is recorded. (iii) As soon as the wires reach the upper side of the membrane and caps start to form, the current increases because of the increasing deposition area. (iv) The current saturates when the caps coalesce to a homogeneous layer and the area does not grow any further.

While the nanowires remained embedded in the template, their crystallinity was studied by means of X-ray diffraction (XRD) using a STOE four-circle diffrac-

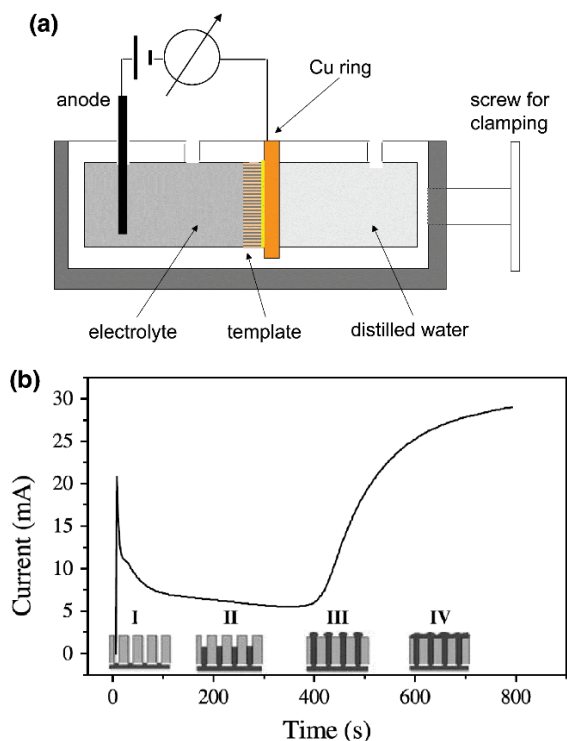


Fig. 8.6 (a) Schematic of the two-compartment electrolytical cell. (b) Deposition current versus time for copper nanowires with diameter 50 nm fabricated at 50°C and -120mV

tometer with graphite monochromatized $\text{Co-K}\alpha$ radiation ($\lambda = 1.7902\text{\AA}$). X-ray diffractograms of gold nanowires deposited potentiostatically at 65°C and different potentials are displayed in Fig. 8.7a. The dashed lines indicate the position and intensity of diffraction signals for a standard gold powder. The wires exhibit a $\langle 220 \rangle$ texture that becomes more pronounced for lower overpotentials during the fabrication process. For wires created at 65°C and -1.2V more than 90% of the crystals are oriented along the $\langle 220 \rangle$ direction. A similar behavior was observed for Cu and Bi nanowires.

The morphology of both nanowires and caps was examined by scanning electron microscopy (SEM) (Philips XL30). SEM images of caps grown on top of the wires that were deposited at 65°C and different overpotentials are depicted in Fig. 8.7b and c. The mean grain size increases with decreasing overpotential and distinct facets are developed. Hence, the cap morphology is a strong indication for the wire crystallinity. The development of texture is based on the different growth rates of various crystal faces. During the deposition process, ad-atoms are attached on the surface of an already existing crystal. Depending on their mobility, they may move to vacant positions of the crystal and build it up further or may act as starting nuclei for a new crystal. Higher mobilities of the ad-atoms lead to a more pronounced tex-

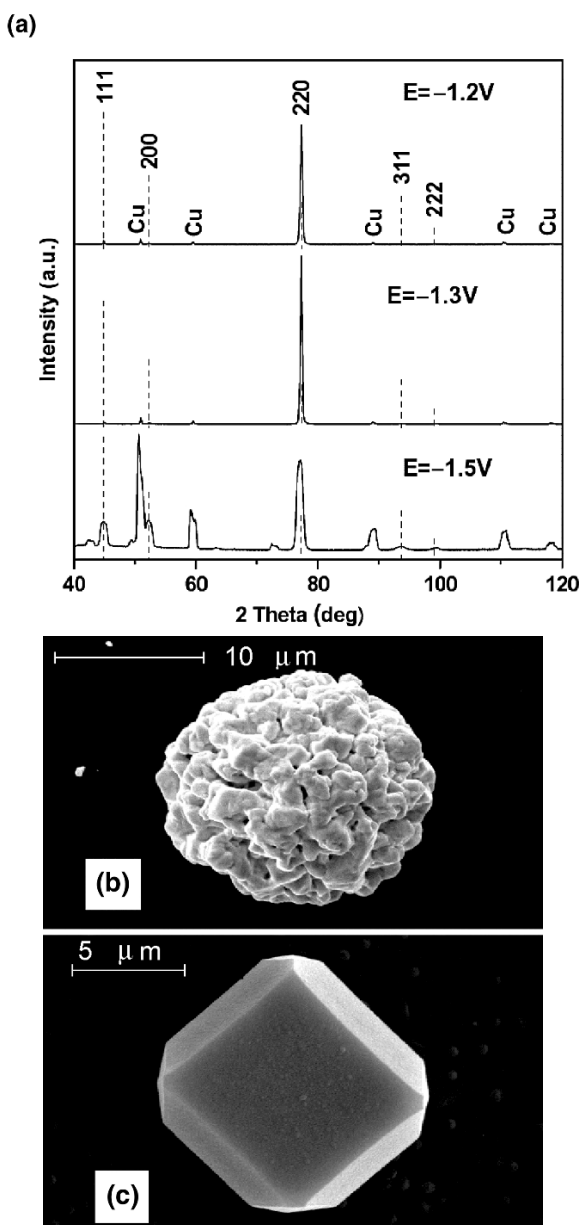


Fig. 8.7 (a) X-ray diffractograms gold nanowires deposited at 65°C and different potentials. SEM micrographs of caps grown on top of Au nanowires deposited at 65°C applying (b) -1.5V and (c) -1.2V

ture. The higher the number of ad-atoms per time on a given surface area, i.e., higher current densities j , the smaller is their mobility because of interaction between them. Larger overpotentials involve larger j . Hence, increased U leads to nucleation and thus to polycrystalline wires.

The crystallinity and crystallographic orientation of the nanowires were also studied by transmission electron microscopy (TEM) (Philips CM20), including selected-area electron diffraction (SAED). For this purpose, the polymer membrane was dissolved in dichloromethane (CH_2Cl_2) and the wires were detached from the back electrode by sonication. Then, few drops of the suspension of the volatile solvent containing clean nanowires were put on a carbon covered TEM grid or, for subsequent IR spectroscopy, on infrared transparent substrates, respectively.

A TEM image and a SAED pattern of a Cu nanowire with diameter 60 nm deposited at 50°C and -45 mV are presented in Fig. 8.8a and b, respectively. The nanowire possesses a smooth contour and a well-defined diameter. The SAED pattern shows regular reflections confirming the single-crystallinity of the wire.

In summary, single crystalline $\langle 110 \rangle$ textured gold and copper nanowires were electrochemically deposited in etched ion-track polycarbonate membranes.

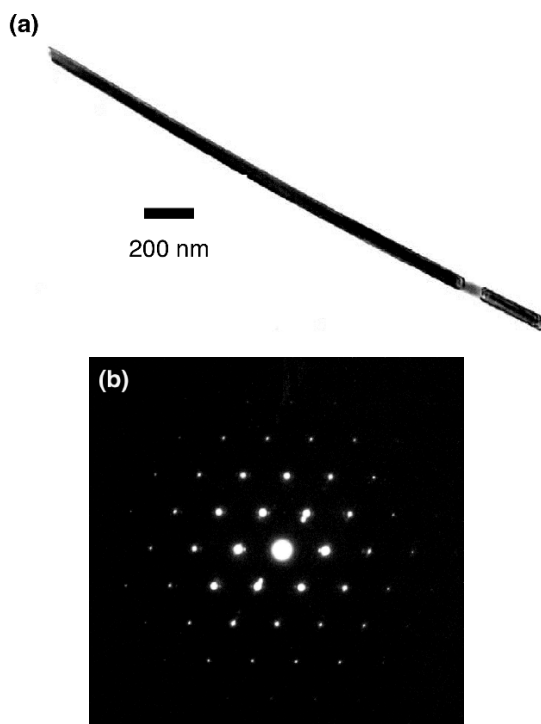


Fig. 8.8 (a) Transmission electron-microscopy image and (b) selected-area electron-diffraction pattern of a copper nanowire with diameter 60 nm

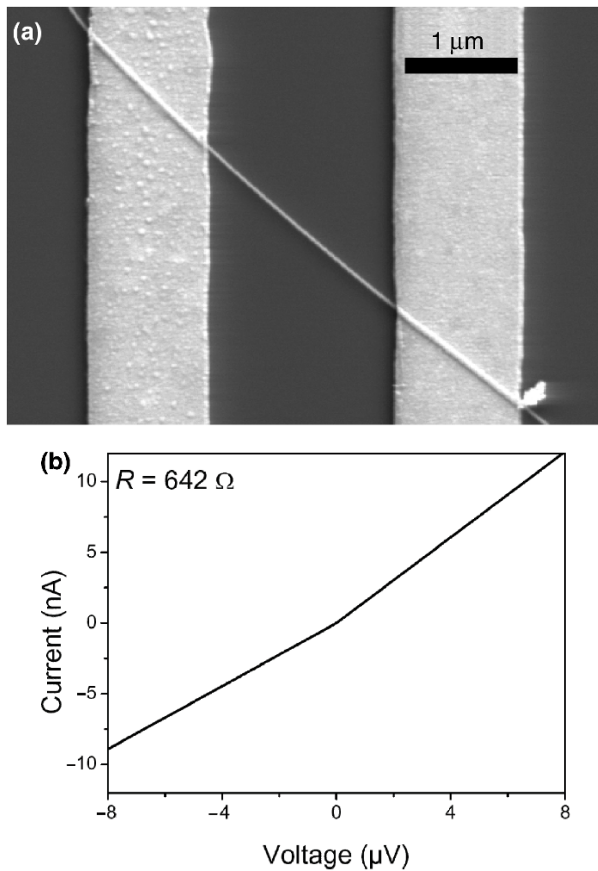


Fig. 8.9 (a) SEM image of a lithographically contacted copper nanowire and (b) the corresponding I - V curve

Electrical transport properties of copper nanowires produced with the same method were studied [68]. The wires were removed from the template, placed on a Si wafer, and contacted lithographically (Fig. 8.9a). The wire resistance showed a linear I - V curve, i.e., it was Ohmic (Fig. 8.9b). The resistance increased with increasing time of exposure to air and, finally, the I - V curve became nonlinear. This behavior was observed at 4.2 as well as at 300 K. The copper wire oxidized to Cu_2O , which behaves like a p-semiconductor. Hence, two Schottky diodes placed back-to-back in series were created at the lithographic contacts, leading to the observed nonOhmic behavior.

To investigate the thermal stability, wires of different diameters were prepared and subsequently annealed at elevated temperatures for a predetermined time period. Cu and Au wires become unstable and fragment at temperatures of few hundred degrees Celsius being far below the bulk melting temperature of 1083 and 1064°C, respectively [61, 62, 69]. An as-prepared gold wire with diameter 25 nm is

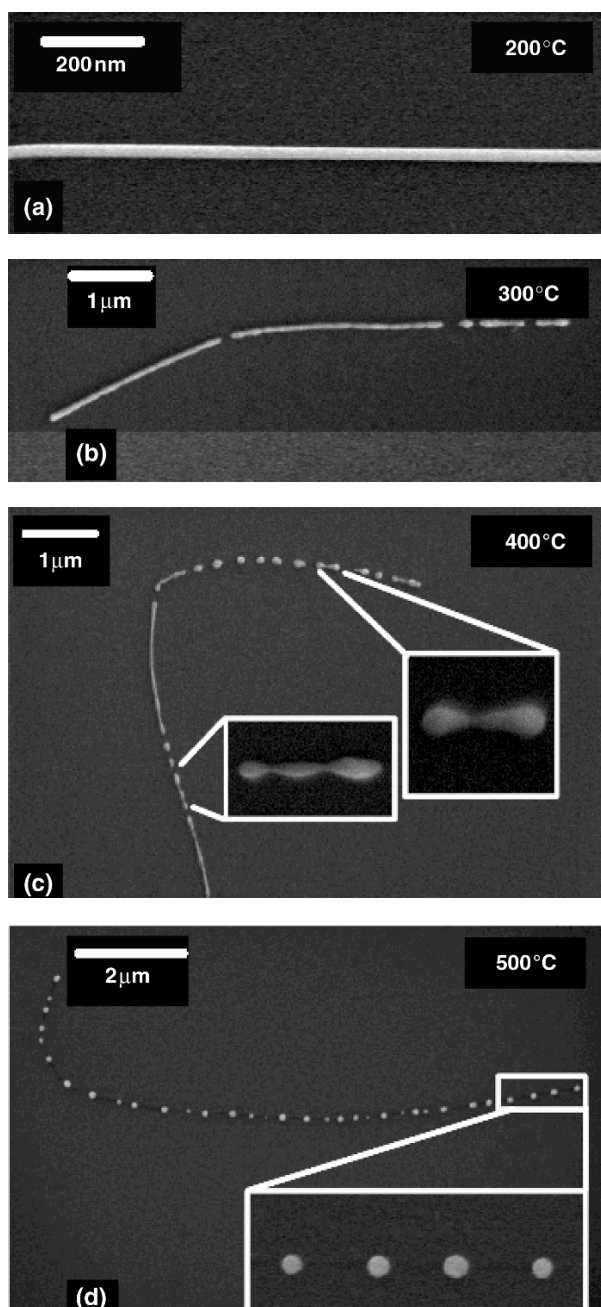


Fig. 8.10 SEM micrographs of (a) an as-prepared wire with diameter 25 nm and (b)–(d) wires after annealing for 30 min at different temperatures

depicted in Fig. 8.10a. Fig. 8.10b–d display SEM images of Au wires after annealing for 30 min at different temperatures. The micrographs reveal different states of the fragmentation process. At 300°C the wires fragment, at 400°C the fragments become oval, and at 500°C the wires are completely transformed into a chain of nanospheres. The driving force of the fragmentation is the so-called Rayleigh instability, i.e., the minimization of the surface energy of the initial cylinder [70]. More than a century ago, Lord Rayleigh described this process for liquid jets. Nichols and Mullins extended the model to solid cylinders by [71]. For the nanowires grown in ion tracks, the distance of adjacent spheres for different wire diameters was found to be larger than predicted by the Nichols and Mullins model. The deviation between experiment and theory originates from the fact that the model assumes an initial cylinder with an isotropic surface energy while solids in general possess crystalline facets and, thus, have an anisotropic surface energy.

8.3.2 Electron-Beam Lithography

Electron-beam lithography (EBL) makes possible the fabrication of nanostructures of desired shape, size, and arrangement.

As shown in Fig. 8.11, to achieve EBL it is necessary to follow different stages.

- 1: The first consists in depositing, by spin-coating, on a glass substrate carefully cleaned the polymer, polymethyl methacrylate (PMMA), whose chains will be broken during the exposure. The thickness of deposited PMMA is about 150 nm. The choice of the PMMA thickness depends on the height of the structures which one wants to design. A ratio 3:1 is generally respected between the thickness of the layer of polymer and the height of the deposited metal.
- 2: The purpose of the second stage is to remove the solvent used, methylisobutylketone (MIBK), from the PMMA film while placing the glass substrate covered with polymer in a drying oven (160°C) during at least 2 h. If the substrate used is glass or another insulator material, it will accumulate the electrons received during the

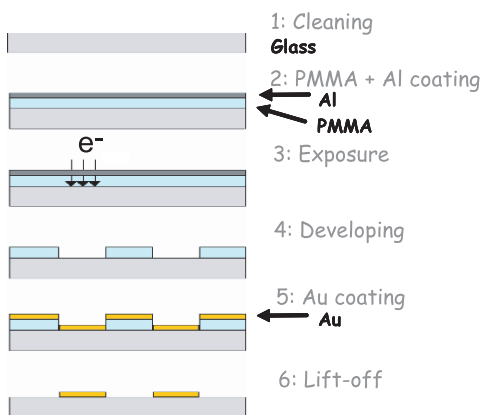


Fig. 8.11 Main stages of the design of a sample by EBL and lift-off techniques

exposure in the scanning electron microscope (SEM). That generates an electric field on the surface of the sample, which disturbs the incident electron beam. To avoid this problem, an aluminum film of 10 nm could be evaporated on the layer of PMMA, thus allowing the dissipation of the charges. That requires an additional stage compared to the use of a conducting substrate like silicon or indium titanium oxide (ITO).

- 3: For exposure with the SEM, it is necessary to use a system of control of the electron beam such as Nanometer Pattern Generation System (NPGS). The designed nanostructures reproduced on the substrate are drawn using a software package as DesignCad LT 2000 and the NPGS system transforms the created nanostructures into a dot matrix. It is then possible to choose the distance between the points to be exposed as well as the distance between lines of points in a very precise way. The coordinates of the points to expose are then transmitted to the system of deflection of the electron beam and to a beam blanker. The exposed zones have typical size from approximately 100 μm .
- 4: For processing, it is necessary to dissolve the layer of aluminum using a solution of potassium hydroxide, KOH. The development can then be carried out. This stage consists of a selective dissolution of the PMMA. Only the exposed zones, having a lower molecular mass, must be dissolved. One usually uses a mixture of 1:3 MIBK and isopropanol (IPA).
- 5: After processing, the metal is evaporated and deposited with the desired thickness on the surface.
- 6: The purpose of the last stage is to dissolve the PMMA remaining on the sample using acetone: the lift-off stage.

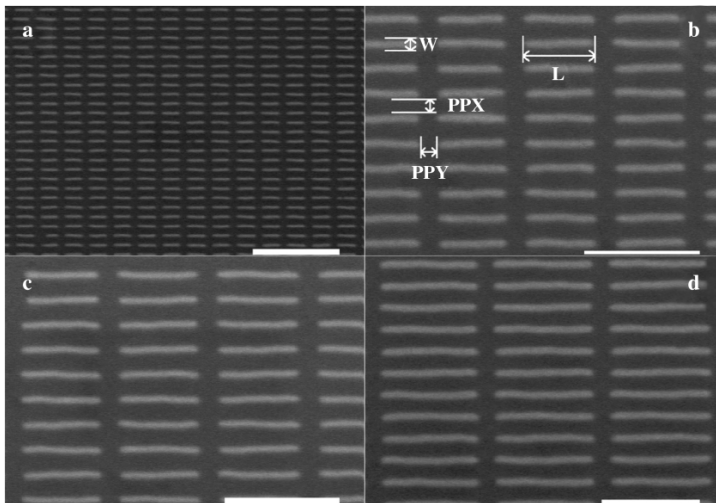


Fig. 8.12 SEM images of arrays of gold nanowires with variable length L (**a**: $L = 420\text{ nm}$, **b**: $L = 620\text{ nm}$, **c**: $L = 720\text{ nm}$, **d**: $L = 1\ \mu\text{m}$), 50 nm height, 60 nm width (W). The gap between nanowires is constant for all arrays and is fixed to 150 nm (PPX and PPY). Scale bars: 2 μm for **a** and 1 μm for **b–d**

This technique provides homogenous arrays of gold or silver nanowires as it can be seen in Fig. 8.12. The limitation of such technique is given by the SEM resolution. It then is not possible to get nanostructures with a size lower than the diameter of the electron beam. Typically, the lowest resolution achieved is few tens of nanometer.

8.4 Spectroscopy of Nanowire Resonances

8.4.1 Infrared Spectroscopy

This subsection reports on the experimental farfield spectroscopy of nanowire resonances of individual metal nanowires prepared by growth in ion tracks, see Sect. 8.3.1, supported by a dielectric substrate in the infrared. Different to studies on ensembles of nanowires [25], one can exclude the influence of wire–wire interaction and averaging over locally varying parameters. Therefore, the experimental results can be compared with existing theories and simulations for individual metal nanowires (see Sect. 8.2.2).

Spectroscopy was performed on metal nanowires prepared by electrochemical deposition in etched ion-track polycarbonate membranes (see Sect. 8.3.1). After fabrication the polymer foil was dissolved in dichloromethane and the clean nanowires were deposited on an infrared transparent substrate, e.g. KBr, ZnS, or CaF₂.

Spectroscopic IR microscopy of single metal nanowires was performed with synchrotron radiation with a higher brilliance compared with conventional IR light sources, e.g. globar. The higher brilliance allows mapping spectral properties of nanowires. Before IR spectroscopy the individual nanowire on the IR-transparent substrate was located by optical microscopy with visible light and its length is determined from those images. Estimating the wire length in this way, a rather big error up to 8% has to be assumed. Operating in the infrared mode of the microscope a circular area of the IR-beam with a diameter of 8.3 μm in the focal plane (sample position) was selected by inserting a circular aperture in the optical path behind the sample. After the IR-beam had been centered on the selected nanowire, IR-transmittance spectra (sample spectra) were recorded. Subsequently, to eliminate effects from beam profile and from substrate inhomogeneities, reference spectra were taken at least 10 μm away from any nanowire and the ratio of sample and reference measurement, called relative transmittance spectrum, is calculated. To determine the lateral position of maximum response of the single nanowire, a grid with a lateral step size of 1 μm is defined and relative transmittance spectra were taken at each grid point. The spectroscopic measurements were done with a Fourier-transform infrared (FT-IR) spectrometer and a LN₂-cooled mercury-cadmium telluride (MCT) detector, which collects light normally transmitted through the sample area. A small fraction of the light scattered away from the normal direction could also be detected because of the collection lens (Schwarzschild objective, numerical aperture: 0.52). This can be neglected in further data analysis because most of the intensity scattered

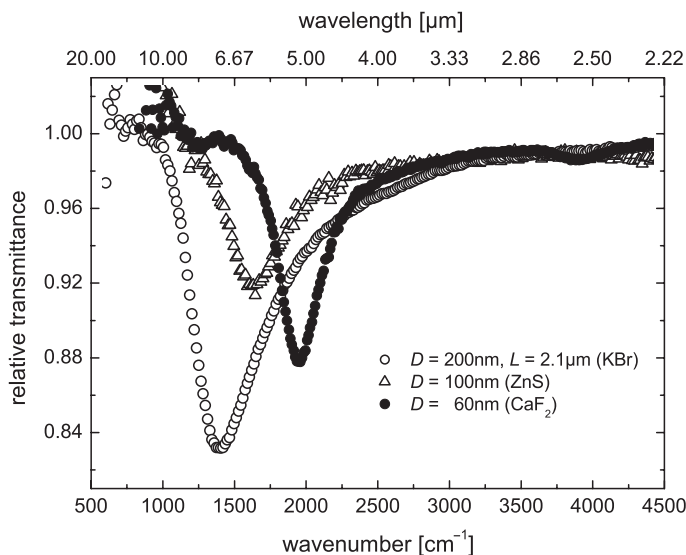


Fig. 8.13 Typical relative transmittance spectra (parallel polarization) of different single gold nanowires with different lengths and diameters (down to 60 nm) placed on different substrates. The fundamental mode of the antennas can be seen clearly

by the nanowire is directed outside the cone of collected light. For both sample and reference measurement IR spectra were recorded by acquisition of at least 10 scans in the spectral range from 600 to 7000 cm^{-1} . A resolution of at least 16 cm^{-1} was sufficient for fundamental nanowire studies because of the spectrally broad response. An even higher resolution of 2 cm^{-1} was used for the SEIRA measurements (see Sect. 6.1). For further analysis of the transmitted light a polarizer was inserted in the optical path before the sample.

The relative transmittance spectra T_{rel} of nanowires (Au, Cu) with a length of a few microns reveal fundamental antenna resonances (see Fig. 8.13). Apart from the fundamental mode much weaker structures of resonant excitation are detected at higher wavenumbers. These modes can be attributed to higher order resonances. Even dipole inactive excitations are observed, which may be due to an electric field component oblique to the long wire axis [72, 73] or bent nanowires. Since the detailed study of higher order resonances of individual wires was hampered by their low signal strength when compared with disturbing effects (beam instability, substrate inhomogeneities), only the fundamental mode of the antenna resonance ($l = 1$ in eq. 8.1) is discussed in the following. The main resonance was only observed for electric field parallel to the long axis of the wire (parallel polarization). For an electric field perpendicular with respect to the long wire axis (perpendicular polarization) the IR-signal was below the noise level, no plasmon was excited.

In Fig. 8.13 the resonance positions (position of minimum transmission) of the different wires depend on length, diameter, and the used substrate. To separate the influence of the length on the resonance frequency, wires with comparable diameters

of about 200 nm placed on KBr are considered (Fig. 8.2b). Assuming the ideal dipole relation as given in eq. 8.1 for a wire completely embedded in vacuum ($n = 1$), a shift of the measured data towards higher resonant wavelengths is obvious. Using the value of the refractive index of KBr in eq. 8.1 the calculated curve seems to fit the measured data. But the used assumption does not fit to the real configuration. The wires are not completely embedded in the substrate, rather they are supported and less than the half of the environment is truly KBr. To get deeper insight, BEM calculations for diameter $D = 200$ nm and variable lengths (L from 1.5 to 4.5 μm) were performed. But, also these calculations do not fit to the data if vacuum around the wire is assumed. Only the BEM calculations for wires embedded in an effective medium with refractive index n_{eff} according to eq. 8.2 yield reasonable agreement to the measured data.

This clearly indicates the influence of the substrate on the resonance position. The polarizability of a cover medium gives further effect. To demonstrate this, individual gold nanowires on different substrates were covered with a thin dielectric layer, e.g. paraffin wax, and IR spectra were taken before and after evaporation. Because of the coverage the resonance wavelength is shifted towards higher wavelengths, which can be estimated with an effective dielectric constant using $\epsilon_{\text{eff}} = \frac{1}{2}(\epsilon_c + \epsilon_s)$ with ϵ_c as the dielectric constant of the cover medium. Together with eq. 8.2 this gives calculated ratios $n_{\text{eff}}^{\text{air}}/n_{\text{eff}}^{\text{paraffin}} = 0.875$ for the KBr substrate (with $\epsilon_s = 2.34$ and $\epsilon_c = 2.02$ for paraffin) and 0.923 for the ZnS substrate (with $\epsilon_s = 4.84$), respectively. These ratios are consistent with the measured data obtained from the spectral shift before and after deposition of paraffin [29].

Comparing experimental nanowire data for Au and Cu, it becomes obvious that the resonance width is proportional to the resonance frequency. This behavior corresponds to that of perfectly conducting cylinders in vacuum [26]. It means that the width of the fundamental resonance in the IR is dominated by the geometry of the nanowire (length L and diameter D), not by its material properties. In the IR the dielectric functions of the metals gold and copper show only marginal quantitative differences and the wire diameters are relatively large compared with the skin depth and to the typical dimensions (a few 10 nm) for the onset of size effects in the conductivity. Deviation could arise if wires are of worse crystalline quality.

From relative transmittance spectra (in Fig. 8.13) the ratio of the extinction cross-section of a single nanowire related to its geometric cross-section was estimated. Assuming $1 - T_{\text{rel}} \approx 2(\sigma_{\text{ext}}/A_0)/(n_s + 1)$, where the influence of the substrate on the signal strength is taken into account in analogy to the transmittance change by the substrate of a thin film [74] in comparison with a freestanding film [75], the ratio

$$\frac{\sigma_{\text{ext}}}{\sigma_{\text{geo}}} \approx A_0(1 - T_{\text{rel}}) \cdot (n_s + 1) \cdot \frac{1}{2LD} \quad (8.6)$$

was obtained. Inserting the spot size A_0 , the transmittance change in the spectrum ($1 - T_{\text{rel}}$), the refractive index of substrate n_s , L from microscopy in the visible spectral range, and D (known from wire growth process) leads to a $\sigma_{\text{ext}}/\sigma_{\text{geo}}$ shown in Fig. 8.14 for a wire with $L \approx 2.37 \mu\text{m}$ and $D = 210$ nm placed on KBr. Any result

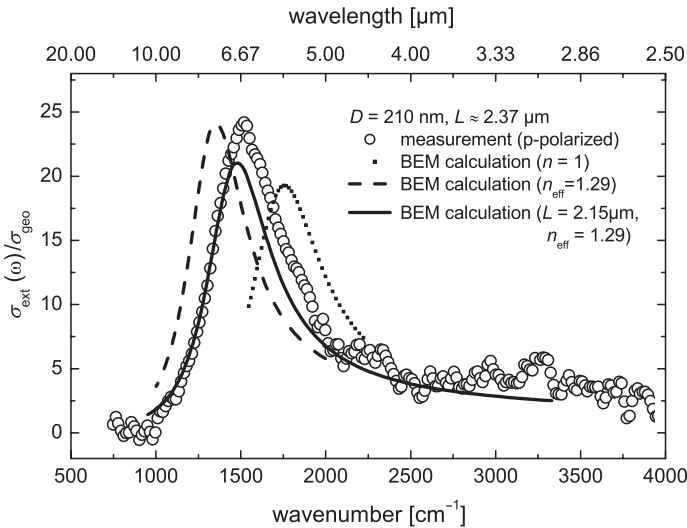


Fig. 8.14 Extinction cross-section related to the geometric cross-section of a gold nanowire with length $L = 2.37\mu\text{m}$ and diameter $D = 210\text{nm}$: experimental data (open circles) and BEM calculations assuming different refractive indices

above 1 means an extinction of intensity above geometric shadowing, which is a clear indication of the nanowires ability to confine light and therefore an indication for an enhanced local field in the vicinity of the nanowire. Since the measurements are performed in the farfield, only a spatially averaged field enhancement factor $\sqrt{\sigma_{\text{ext}}/\sigma_{\text{geo}}}$ can be calculated. For the representative spectrum in Fig. 8.14 a farfield enhancement factor of about 5 can be estimated for the resonance position.

The calculated resonance curves of single gold nanowires in Fig. 8.14 are obtained using the boundary element method BEM (see Sect. 8.2.2). Here, the gold nanowire is modeled as a rod with hemispherical tip ends completely embedded in a medium. As discussed in Sect. 8.2, the calculated data for a nanowire in vacuum deviate from the experimental ones because of the polarizability of the substrate. Considering an effective refractive index $n_{\text{eff}} = 1.29$ (according to eq. 8.2) in order to describe the influence of the substrate approximately, an even better agreement in strength and shape of the resonance curve with the experimental data is obtained. Only the position of the resonance maximum differs slightly. But, a BEM calculation with a length changed within its error fits the measured spectrum data. The same does a calculation (not shown) with an unchanged length but a slightly different n_{eff} of 1.20. At this point the wire-length uncertainty for this sample type limited a more precise conclusion.

The important role of the substrate polarizability was also discussed by Fumeaux [76] who studied the resonance length of gold nanoantennas for two fixed IR wavelengths and one in the visible range with a special microbolometer setup.

8.4.2 Antenna Resonances in the Visible Range

In the visible to ultraviolet range, below the optical plasma edge of the respective metal, several types of plasmon resonances of metal nanowires can be observed. These are the resonances for electric field along the short axis of nanowires, antenna resonances (LSP) of accordingly short nanowires, and higher orders of antenna resonances from wires with micron length.

The LSP resonance position is strongly dependent on the detailed particle shape. For fixed length that resonance is red-shifted with diameter, and, as shown in Fig. 8.15, this shift could be of several tens of nanometers and even more when the size of the nanoparticle increases [2,35,77]. For an ellipsoidal particle the redshift is faster than for a cylindrical particle as shown in Fig. 8.15. For an increase of 10 nm in size, the shift of the LSP for an ellipse (e-beam lithographically written structure with certain height) is of 30 nm whereas it is only of 10 nm for a cylinder-like structure [2].

The plasmon resonances were measured by extinction (all the losses due to scattering and absorption) spectroscopy in transmission. The e-beam lithographically prepared samples (Sect. 8.3.2) were illuminated at normal incidence with collimated white light polarized along the nanowires length. To take into account the optical transfer function of the experimental set-up (different optical transmission for each wavelength due to the mirrors, the array or the CCD), it was necessary, in a first stage, to record the intensity of the light transmission without the nanowires (I_0). In a second stage, the intensity of the light transmission is measured considering the presence of the nanowires (I_t). The nanowire spectrum corresponding to

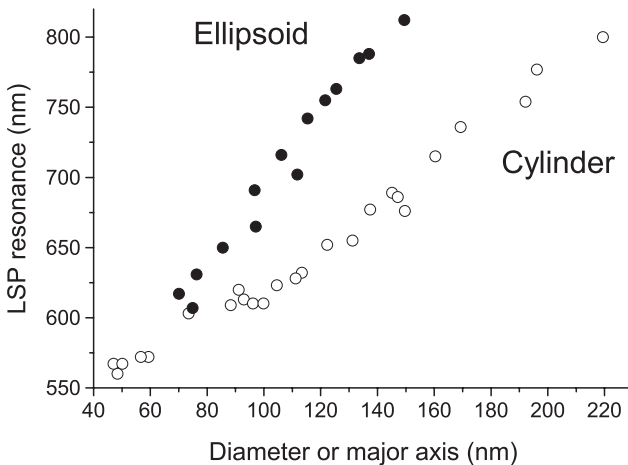


Fig. 8.15 Variation of the LSP resonance wavelength with diameter of cylinder-like structures (open circle) or with length of ellipse-like structures (full circle), respectively. The minor axis of the ellipsoids is 50 nm and the height of the two kinds of nanoparticles is 50 nm. The gap between two nanoparticles is kept constant at 200 nm. The particles were made by electron-beam lithography on glass

the plasmon resonance was obtained by simply dividing I_0 by I_t , i.e. it is shown as $(T_{\text{rel}})^{-1}$. Since the experiments were done in transmission configuration, it implies that the nanowires had been deposited on a transparent substrate such as glass or ITO.

Extinction spectra were recorded on a Jobin–Yvon micro-Raman spectrophotometer (Labram) [78]. Each extinction spectrum was recorded, by removing the notch filter, over an area of $80 \times 80 \mu\text{m}^2$ in diameter selected by the confocal hole. A 10-fold magnification objective (NA = 0.28) was used. It was important to use an objective with a small numerical aperture (NA) since only the transmitted light should be collected and not the light diffusely scattered by the nanowire. The use of nanoparticle arrays was necessary to get enough signal strength since the extinction signal of isolated nanoparticles was too low with such experimental set up. (It has to be noticed that the antenna resonances in the visible range are much weaker than in the infrared.) With scanning nearfield optical microscopy individual nanoantennas can be studied, however, still with less energy resolution than in farfield spectroscopy.

Higher orders of resonance of longer nanowires can be observed as new bands in extinction spectra at wavelengths considerably lower than the dipolar LSP resonance, as shown in Fig. 8.16. Thus, on the spectra, when one resonance band is

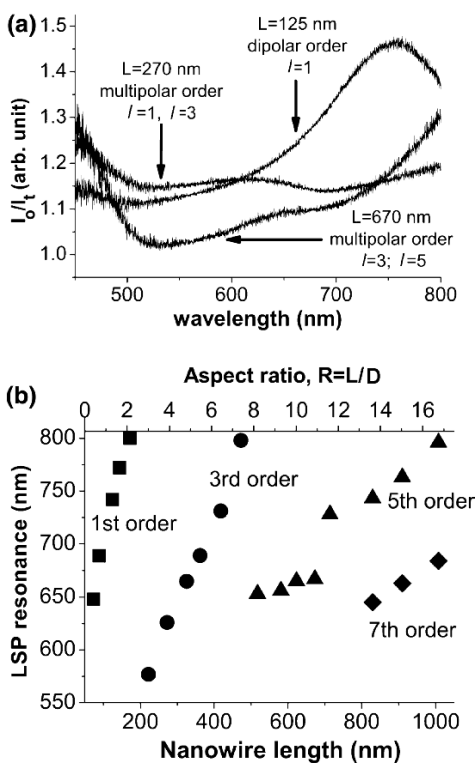


Fig. 8.16 (a) Extinction spectra I_0/I_t of electron-beam lithographically made gold nanowires arrays of different lengths L on glass. The value of l represents the LSP order. (b) Development of the LSP resonance with nanowires length L and respective aspect ratio (in the array plane) of the nanowire (ratio R between L and the width of the nanowires): 1st order (square), 3rd order (circle), 5th order (triangle), 7th order (diamond). The width and height of the nanowire, and the gap between two nanowires were kept constant at 60, 50, and 150 nm, respectively

red-shifted because of an increasing length, another one appears in the low wavelength range and is also red-shifted when the length of the nanowire further increases [79]. Schider et al. have assigned these multiorder resonances to odd orders l ((1)) because the resonance should keep the same symmetry than the nanowire [4]. With nanowires up to $1\ \mu\text{m}$ long, we can observe up to the 7th order, as shown in Fig. 8.16. In the case of multiorder resonances, it should be noticed that the red shift is not identical for each order, but the variation the LSP resonance position is lower for higher order [4, 31, 72, 73, 79].

For nanowires longer than $1\ \mu\text{m}$, Féliidj et al. were able to observe some multiorder resonances and the associated local maxima by Raman imaging [80]. They have then measured a LSP beat wavelength of 379 nm. Moreover, Ditlbacher et al. have proposed to consider the nanowires as LSP resonators [81]. In the case of nanowires longer than $10\ \mu\text{m}$, they have been able to determine a propagation length of about $10\ \mu\text{m}$ and a nanowire end face reflectivity of 25%. They assume that the nanowire can be applied as efficient LSP Fabry–Perrot resonator.

Another application takes advantage of the fact that the position of the LSP resonance is both, different for each of the three nonidentical dimension of the nanowire along their respective directions and strongly dependent on the polarization of the exciting field. It is the design of a spectral selective polarizing nanowire device for the visible range proposed by Schider et al. The authors of this work optimized the extinction ratio between TE and TM polarization through the use of a nanowire grating and the selection of the appropriate grating parameters and nanowire width [82]. In the IR similar metal-grating polarizers are in practical use since many years.

8.5 Application to Surface Enhanced Raman Scattering

The surface enhanced Raman scattering (SERS) is a powerful tool that has made possible the observation of small numbers of molecules. Moreover, it has allowed the observation of individual molecules because of a Raman signal enhancement estimated to 10^{14} [54, 83].

This important intensification of the Raman signal is achieved by using some metallic nanostructures such as nanoparticles, rough thin films, colloidal solutions, etc. The origin of the Raman scattering enhancement can be interpreted in terms of two different processes: the first one of electromagnetic nature [23, 84] and the second process with chemical origin [85, 86].

The electromagnetic process is based on the nearfield interaction between a metallic “particle” (Au, Ag, Cu...) and a molecule. During the illumination of the SERS surface at the excitation wavelength λ_0 , the particle interacts with light and creates a significant local enhancement of the electromagnetic field that can be achieved under specific conditions: plasmon resonance, lightning rod effect, or confinement effect. Therefore, a molecule in the vicinity of the resonant particle is excited because of a huge field. Since the Raman process is proportional to the excitation field, the molecule scatters a large Raman signal at a shifted wavelength

λ_R . The Raman wavelength can also interact with the particle (re-radiation process) and be enhanced. Thus, the enhancement factor can be written as [23]:

$$\left| \frac{E_{\text{local}}(\lambda_0)}{E_0(\lambda_0)} \right|^2 \left| \frac{E_{\text{local}}(\lambda_R)}{E_0(\lambda_R)} \right|^2 = f(\lambda_0)f(\lambda_R) \quad (8.7)$$

The first term, at λ_0 , stems from the particle nearfield enhancement at the incident wavelength. The second one, at λ_R , arises from the re-radiation of the molecule Raman nearfield by the particle. As a rough approximation it is assumed that the Raman enhancement is proportional to the fourth power of the nearfield local enhancement around the particles. Then a field enhancement factor of 10^3 induces a Raman enhancement of 10^{12} . That simple approximation is not completely valid since the spectral shift between the incident and Raman wavelength can be important (several tens of nanometers). Then the position of the Raman wavelength has an influence on the signal enhancement [2, 87].

The chemical enhancement is less understood. However, it is often explained in terms of the electronic interactions between metal surface and molecules adsorbed to certain defect sites. Some models proposed a dynamic charge transfer (Otto 1983 [86, 88–90]). Unified treatments for Raman and fluorescence have also been developed to account for the quantum-mechanical process in a metallic electro-dynamical environment [91, 92]. The contribution of such process to SERS enhancement has been estimated to two orders of magnitude. That means that the chemical process does not contribute significantly to the Raman signal enhancement. Therefore and since it is observed only in case of special atomic defects on the metal surface, we will focus on the electromagnetic enhancement here. In contrast to the control of the chemical effect [93], it is much better known how the electromagnetic field enhancement can be manipulated in a controlled manner, which is still under investigation for the first layer effect [93].

The precise determination of the SERS efficiency of a nanostructured substrate and its relation to the optical properties of the substrate requires the control of size and shape of the nanostructures. For this, several groups have used lithographic techniques such as e-beam lithography (see Sect. 8.3.2) or nanosphere lithography to design some nanoparticle arrays [1, 2, 87, 94–96]. Chemical self-assembly has also been used to produce such arrays [97]. In these cases, one can control precisely the position of the plasmon resonance of the nanoparticle. It is then possible to estimate the role of the plasmon resonance on the Raman signal enhancement.

Since there are two different enhancement factors at the incident and Raman wavelengths, λ_0 and λ_R , one would intuitively assume that the best Raman signal is obtained for a position of the plasmon resonance located between the two wavelengths λ_0 and λ_R . Indeed, this has been observed for cylindrical (Fig. 8.17) or triangular nanoparticles with a maximum of enhancement achieved for a plasmon resonance close to $(\lambda_0 + \lambda_R)/2$ [2, 87, 94, 96].

For the results shown here, SERS-active substrates were obtained by immersion in a 10^{-3} M solution of the probe molecule, *trans*-1,2-bis(4-pyridyl)ethylen (BPE), during 1 h and drying with nitrogen. Raman spectra are recorded on a Jobin–Yvon

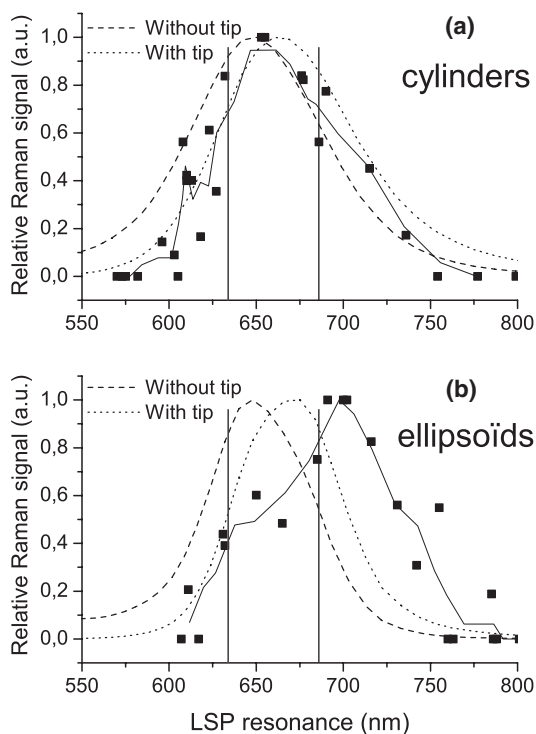


Fig. 8.17 Raman signal enhancement versus LSP resonance: **(a)** for cylinder-like structures, **(b)** for ellipse-like structures, both as in Fig. 8.15. The enhancement has been estimated from the intensity of the 1200 cm^{-1} line of the *trans*-1,2-*bis*(4-pyridyl)ethylene used as molecular probe and the LSP resonances correspond to the ones observed in Fig. 8.15. Solid lines are the binned average values of the LSP resonance and the Raman intensity. The dashed and dotted lines are the Raman signal enhancement calculated in the quasistatic approximation without the lightning rod effect of the tip (dashed line) and with that effect (dotted line), respectively. The minor axis of the ellipsoids is 50 nm and the height of the two kinds of nanoparticle is 50 nm. The gap between two nanoparticles is kept constant at 200 nm. The excitation wavelength was the 632.8 nm line of an He–Ne laser. The excitation wavelength and the Raman wavelength are marked with vertical lines

micro-Raman spectrophotometer (Labram). For Raman spectroscopy a $100\times$ magnification objective ($NA = 0.90$) in back scattering geometry was used. Raman measurements were carried out with the 632.8 nm line of an He–Ne laser. To actually determine the effect of the nanowire length on the Raman enhancement, the laser polarization was fixed for all experiments relatively to the long axis of the nanowires. Even if the chosen microscope objective has a large numerical aperture ($NA = 0.90$), the laser beam depolarization was small and not significant [98, 99]. Thus, only a small amount (a few percent) of the total energy of the excitation light was depolarized. Moreover, this depolarized light was not located on the central focus spot but laterally [98, 99]. It was easily eliminated with an appropriate confocal hole. The intensity of the signal was estimated by calculating the area of a Lorentzian fitted band of *trans*-1,2-*bis*(4-pyridyl)ethylene located at 1200 cm^{-1}

(this mode has significant ethylene C = C stretch character, see [100] for details). To see the role of the nanowire characteristics (length, plasmon resonance, etc.) on the SERS signal, only the relative Raman intensity is considered. Accordingly, for each figure of this section, the collected Raman signal was normalized to the best Raman signal obtained with nanowires.

Different to the cylinders, in the case of ellipsoidal nanoparticles Fig. 8.17 shows the best enhancement for the plasmon resonance close to the Raman wavelength λ_R [2]. This result can be explained with a simple quasistatic model, which allows the determination of the position of the plasmon resonance and the Raman signal enhancement [2]. The authors of this work have shown that depending on whether the lightning rod effect due to the wire tip is taken account or not, the LSP resonance required to achieve the best Raman signal enhancement will be shifted or not shifted, respectively. That is, this LSP resonance is red-shifted and close to the Raman wavelength when this tip effect is introduced in the model whereas it is still located between the two wavelengths λ_0 and λ_R if this tip effect is not considered, as shown in Fig. 8.17 [2]. In this case, one can assume that the process of Raman re-radiation seems to be more favored because of the lightning rod effect and, therefore, for elongated particles that play the role of a nanoantenna [2].

To determine the effect of nanoparticles with high aspect ratio on the Raman enhancement, several research groups have studied gold nanowires and their SERS efficiency [11, 31, 72, 73]. Laurent et al. have shown that nanowires with lengths from 200 nm to 650 nm are also active as SERS substrates and that such structures are also relevant to make SERS experiments [72, 73]. It means that the higher (multi)-order LSP observed with long nanowires are also efficient for SERS as could be dipolar modes. The effect of the multiorder LSP modes was demonstrated by Billot et al. [31]. In this reference, it is shown how the Raman signal enhancement is strongly dependent on the length of the nanowire. As depicted on Fig. 8.18 the Raman signal shows a strong variation with the length of the nanowire. Three maxima can be observed on such curve between 100 and 200 nm and about 650 and 900 nm. The size and shape of the nanowire seem to be of real importance to determine the best Raman signal enhancement.

The SERS gains were calculated with the three-dimensional finite-difference time-domain (FDTD) method using the Drude–Lorentz dispersion model. The Raman signal enhancement is determined at the surface of the nanoparticles and molecules are considered as polarizable point dipoles homogeneously distributed at the particle surface (for more details on the model, see [101, 102]).

The FDTD method gives a good agreement with the experimental data as shown in Fig. 8.18. From the enhancement mapping around the nanowire, these calculations make obvious that the Raman enhancement is highly located at the tip end of the nanowire and that the main contribution to the Raman signal enhancement comes from the two extremities of the nanowire [31].

To confirm this observation, the results can be compared qualitatively to some other numerical calculations done by Calander et al. [103]. Indeed, Calander et al. [103] have calculated the field enhancement at the tip of silver ellipses with length up to 1.6 μm and aspect ratio up to 25. They observed some maxima of field enhancement for specific lengths and aspect ratios. There are especially three zones

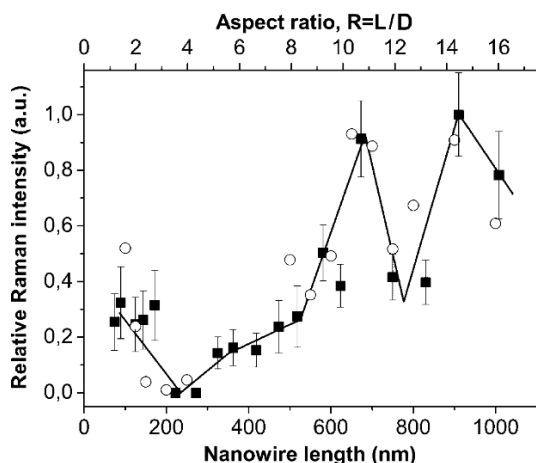


Fig. 8.18 Evolution of the Raman signal enhancement versus the nanowire aspect ratio R and the nanowire length for experimental data (plain square) and for FDTD calculations (open circle). The enhancement has been estimated from the intensity of the 1200 cm^{-1} line of the *trans*-1,2-bis(4-pyridyl)ethylene used as molecular probe. The plain line is just a guide for the eyes. The width and height of the nanowire and gap between two nanowires are kept constant at 60, 50, and 150 nm, respectively. The excitation wavelength was the 632.8 nm line of an He–Ne laser

of maxima for lengths about 50, 500, and 1000 nm and respective aspect ratios 5, 10, and 14. Although the authors of these references do not use the same materials (gold [31] and silver [103]), one could suppose that the results obtained for these two different metals should be close since their dielectric functions are rather similar at the excitation wavelength of 633 nm used in both papers. The importance of these results lies on the fact that they point out the crucial role of the size and the shape of the nanowire in the determination and optimization of their SERS efficiency.

To go further and to determine the plasmon resonance contribution, the Raman signal enhancement can also be plotted versus the plasmon resonance position (Fig. 8.19). This has been done for each plasmon order since multiorder LSP modes are observable for nanowires with length above 200 nm (see Sect. 8.4.2 and notice that the nanowires used for SERS experiments presented in Fig. 8.19 are the same for which the LSP resonance has been shown in Fig. 8.16). To choose the plasmon resonance order, the plasmon resonance used was the closest to the excitation wavelength (633 nm). In this case, the best enhancement is achieved for the 5th and the 7th order, which means that in specific conditions the higher order LSP modes can give better enhancement than dipolar order [31]. Moreover, another interesting result is that for almost each order, the best enhancement is obtained for a plasmon resonance close to the Raman wavelength [31]. This means that even for higher-order LSP modes, the best SERS efficiency is achieved for a LSP resonance close to the Raman wavelength. This latter observation seems to be a general rule that can be applied to either dipolar or multiorder LSP modes. Regarding the interpretation given for small ellipses and for the dipolar modes, the nanowire can be considered, independently of its length, as an optical nanoantenna.

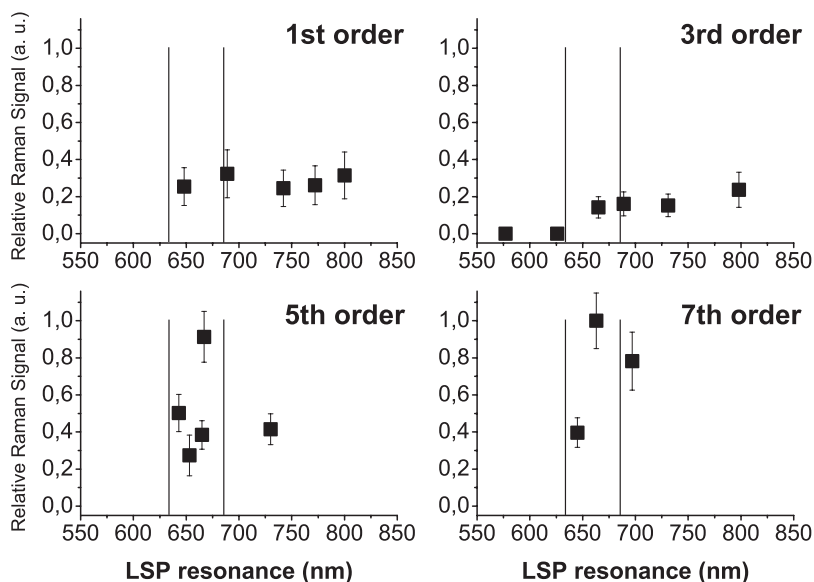


Fig. 8.19 Evolution of the Raman signal enhancement versus the LSP resonance for each order observed in Fig. 8.16. The enhancement has been estimated from the intensity of the 1200cm^{-1} line of the *trans*-1,2-bis(4-pyridyl)ethylene used as molecular probe. The excitation wavelength and the Raman wavelength are marked with vertical lines

8.6 Application to Surface Enhanced Infrared Spectroscopy

In 1980, Hartstein et al. [104] found that the IR absorption of molecules can be enhanced. The enhancement factor can reach the order of 1000, if the molecules are adsorbed on Au or Ag island films. [105–107 and references therein].

This effect was called surface enhanced infrared absorption (SEIRA). As explained earlier for antennas, the strength of the enhancement depends on the metal type according to the specific dielectric function in the infrared and, because of the relation to the excitation spectrum of surface plasmons in the IR range, on the metal-film morphology. Also to SEIRA may contribute a first-layer effect [108], which is not considered here. For metal-island films, maximum enhancement is found at the percolation threshold [109]. Model calculations based on effective dielectric functions are able to describe the experimental results from IR transmittance spectroscopy of extended film areas well. However, it is important to note that the real film morphology must fit to the assumptions of the model [110]. Such model calculations revealed enhanced adsorbate-vibration signals but also a change in the adsorbate lineshape with metal-filling factor of the film [109]. The lineshape may be strongly asymmetric [111]. The strongest asymmetry occurs at the percolation threshold at which the enhancement reaches the maximum [109]. Looking at the individual metal islands this maximum enhancement can be understood well, since at percolation the number of adsorbate sites in the smallest possible grooves between

neighbor islands becomes maximum. In these grooves the local field enhancement $|E_{\text{local}}(\lambda_{\text{IR}})/E_0(\lambda_{\text{IR}})|$ is expected to be particularly strong. For random film morphologies certain hot spots with huge field enhancement are mentioned in the SERS literature, for example [112]. There is no reason why they should not exist in the IR range.

The local adsorbate-vibration signal enhancement can be estimated as $|E_{\text{local}}(\lambda_{\text{IR}})/E_0(\lambda_{\text{IR}})|^2$, the detailed lineshape change was not considered. The signal enhancement (or the enhancement factor, respectively) depends on the electromagnetic resonance spectrum in the nearfield. Since the islands usually are rather flat and broad and since they have a strong electromagnetic coupling to neighbor islands such resonance curves in the IR are extremely broadened. The oscillator strength of these broad resonances depends on size, shape, and the kind of array on the one hand, and, on the other hand, on the metallic properties of the particles; for example, on the relaxation rate of the free charge carriers and on their plasma frequency. The enhancement therefore depends strongly on the metal properties [113]. In reality this means also, that too small particles give less enhancement because of the strong effect of surface scattering of free charge carriers.

SEIRA studies of extended areas of metal-nanoparticle films always give only information on the average enhancement [113]. The best average enhancement factors are only three orders of magnitude [106], since higher local enhancement is balanced with lower ones at adsorption sites in wider grooves or at smaller islands.

In the following we will show one attempt to get an information on the possible local enhancement factor for molecules on an individual object; here a nanowire.

The enhanced farfield cross-section of a single nanowire at resonance mentioned in Sect. 8.4.1 already indicates the enhanced nearfield in the vicinity of the nanowire tips. Moreover, theoretical calculations (with use of BEM) reveal the enhanced nearfield for a nanowire oscillating in resonance (e.g. for a wire with $L \approx 2.37 \mu\text{m}$ and $D = 210 \text{nm}$ in vacuum) to be $|E_{\text{local}}/E_0| \approx 30$ at a distance of 5 nm from the tip end of the wire. Even higher enhancement should be achieved for closer distances to the tip. To detect the enhanced nearfield experimentally, an adsorbate molecule is used as probe. The well-known molecule octadecanethiol (ODT), which is an organic compound containing one thiol (SH) group as a functional group, is adsorbed. Concerning SEIRA, the usage of the long-chained ODT ($\text{C}_{18}\text{H}_{37}\text{SH}$) provides three advantages: (i) it easily adsorbs on noble metals because of the particular affinity of sulfur, which ensures a well-defined sample preparation (e.g., ODT only adsorbs on gold surfaces, like films or wires, and not on the surface of the substrate). This fact is well known from preparation of self-assembled monolayers (SAM) [114]. (ii) The surface of an ODT monolayer is very inert preventing multilayer absorption; a well-defined thickness (2.4 nm [115]) of the ODT monolayer is feasible. (iii) ODT features several infrared active absorption modes. The IR spectrum of ODT reveals absorption bands because of the vibration of methyl (CH_3) and methylene (CH_2) groups. For the investigations in the following the strongest absorption modes of these groups (symmetric (2919cm^{-1}) and asymmetric (2850cm^{-1}) CH_2 stretching vibrations [116]) are considered.

The sample preparation is rather common. Single gold nanowires are deposited on an infrared-transparent substrate (CaF_2) and exposed to a 1 mM solution of ODT in ethanol for at least 8 h. After such long deposition time one can be sure that one monolayer of ODT is adsorbed on the gold nanowires. To obtain an absorption band of ODT close to the fundamental resonance of the nanowire, a nanowire with an appropriate length has to be chosen. After localizing such a wire by microscopy with visible light, normal IR transmittance measurements under the same conditions as described in Sect. 8.4.1 are performed. Sample spectra are recorded at the position of the selected gold nanowire covered with ODT, reference spectra are taken at a position beside the nanowire without ODT (see Fig. 8.20). The relative transmittance of the selected single nanowire (diameter 100 nm) reveals the fundamental antenna resonance. In addition absorption bands at 2850 and 2919 cm^{-1} , which can be identified as symmetric and asymmetric CH_2 stretching vibrations of ODT (see Fig. 8.21, black line), are detected in the infrared spectrum. In the case of gold wires

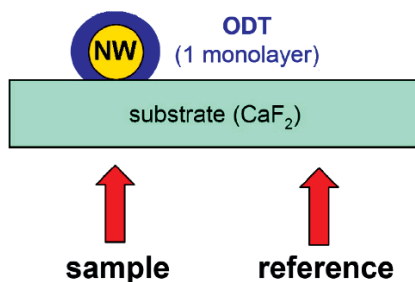


Fig. 8.20 Sketch of the applied measurement principle

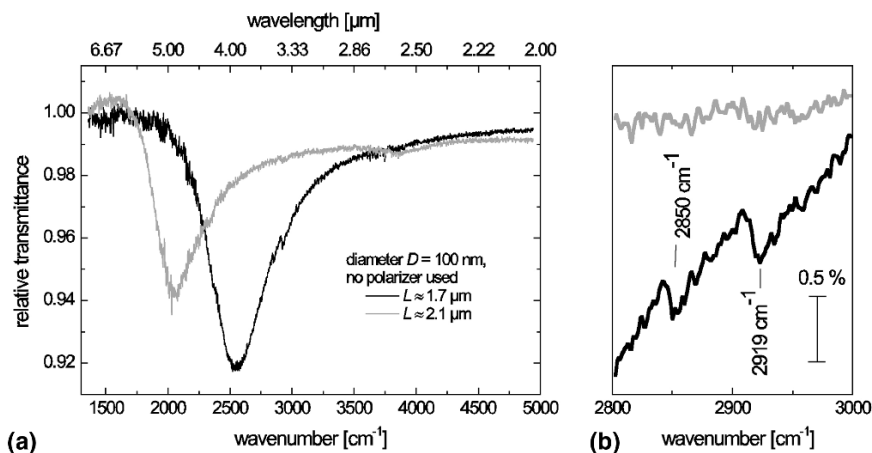


Fig. 8.21 (a) Relative transmittance spectra of two different single gold nanowires covered with one monolayer ODT. (b) Magnification: The absorption bands can be assigned to the stretching vibrations of CH_2 for the wire with resonance frequency in the range of these vibrations (black line). For the wire with resonance frequency at lower wavenumbers no absorption bands are detected (grey line)

with antenna resonances at much lower resonance frequency than the CH_2 stretching modes of ODT these vibrations could not be observed (grey line). The appearance of the absorption bands of one monolayer ODT on a single nanowire is an indication of local field enhancement due to the antenna resonance. As it follows from the spatial distribution of the local field enhancement around a nanowire at resonance, the detected signal should mainly originate from the molecules adsorbed on the wire tips. Also, the contributions to the signal from ODT molecules adsorbed elsewhere are suppressed by mirror charges at the nanowires surface or the absorption modes cannot be excited because of the orientation of their dynamic dipole perpendicular to the exciting field. The nearfield enhancement can be estimated by comparing the antenna-enhanced symmetric CH_2 absorption band to the nonenhanced symmetric CH_2 absorption band achieved from infrared reflection-absorption spectroscopy (IRRAS) measurements of ODT on smooth gold films [117]. Taking into account the areas that really contribute to the signal (the hole sample area in IRRAS, for the SEIRA spectrum the tip ends from the individual nanowire as a small part of the focal area), the SEIRA-factor was estimated to reach 100,000 for the spectrum in Fig. 8.21. Even higher enhancement is achieved if the resonance wavelength is exactly at the molecular vibration [117].

Acknowledgments F.N. and A.P. gratefully acknowledge technical support by M. Süpfle, helpful discussions with A. Otto, B. Gasharova, and Y.-L. Mathis. J.A. acknowledges software access from F.J. García de Abajo, discussions with G.W. Bryant, and financial support from Gipuzkoa Foru Alundia (Gipuzkoa Fellows program) and the Government of the Basque Country (NANOTRON project).

References

1. Félidj N, Aubard J, Lévi G, Krenn JR, Salerno M, Schider G, Lamprecht B, Leitner A, Aussenegg FR (2002) Controlling the optical response of regular arrays of gold particles for surface-enhanced Raman scattering. *Phys Rev B* 65:075419
2. Grand J, Lamy de la Chapelle M, Bijeon JL, Adam PM, Vial A, and Royer P (2005) Role of localized surface plasmons in surface-enhanced Raman scattering of shape-controlled metallic particles in regular arrays. *Phys Rev B* 72:033407
3. Link S, El-Sayed MA (1999a) Spectral properties and relaxation dynamics of surface plasmon electronic oscillations in gold and silver nano-dots and nano-rods. *J Phys Chem B* 103:8410
4. Schider G, Krenn JR, Hohenau A, Ditlbacher H, Leitner A, Aussenegg FR, Schaich WL, Puscasu I, Monacelli B, and Boreman G (2003) Plasmon dispersion relation of Au and Ag nanowires. *Phys Rev B* 68:155427
5. Anger P, Bharadwaj P, Novotny L (2007) Spectral dependence of single molecule fluorescence enhancement. *Nanotechnology* 18:044017
6. Farahani JN, Pohl DW, Eisler HJ, Hecht B (2005) Single quantum dot coupled to a scanning optical antenna: A tunable superemitter. *Phys Rev Lett* 95:017402
7. Frey HG, Witt S, Felderer K, Guckenberger R (2004) High resolution imaging of single fluorescent molecules with the optical near-field of a metal tip. *Phys Rev Lett* 93:200801
8. Mertens H, Biteen JS, Atwater HA, Polman A (2006) Polarization-selective plasmon-enhanced silicon quantum-dot luminescence. *Nano Lett* 6:2622

9. Girard G (2005) Near fields in nanostructures. *Rep Prog Phys* 68:1883
10. Mie G (1908) Beiträge zur Optik trüber Medien, speziell kolloidaler Metallösungen. *Ann Phys, Lpz* 25, 377
11. Aizpurua J, Bryant GW, Richter LJ, García de Abajo FJ, Kelley BK, Mallouk T (2005) Optical properties of coupled metallic nanorods for field-enhanced spectroscopy. *Phys Rev B* 71:235420
12. Cubukcu E, Kort EA, Crozier KB, Capasso F (2006) Plasmonic laser antenna. *Appl Phys Lett* 89:093120
13. Ebbesen TW, Lezec HJ, Ghaemi HF, Thio T, Wolff PA (1998) Extraordinary optical transmission through sub-wavelength hole arrays. *Nature* 391:667
14. Bozhevolnyi SI, Volkov VS, Devaux E, Laluet JY, Ebbesen TW (2006) Channel plasmon subwavelength waveguide components including interferometers and ring resonators. *Nature* 440:508
15. Fan S, Joannopoulos JD (2002) Analysis of guided resonances in photonic crystal slabs. *Phys Rev B* 65:235112
16. Steinhögl W, Schindler G, Steinlesberger G, and Engelhardt M (2002) Size-dependent resistivity of metallic wires in the mesoscopic range. *Phys Rev B* 66:075414
17. Berthier S, Peiro J (1997) Infrared absorption of nanocermetts close to the percolation threshold. *J Phys III (France)* 7:537
18. Jackson JB, Halas NJ (2004) Surface-enhanced Raman scattering on tunable plasmonic nanoparticle substrates. *Proc Natl Acad Sci USA* 101:17930
19. Shubin VA, Sarychev AK, Clerc JP, and Shalaev VM (2000) Local electric and magnetic fields in semicontinuous metal films: Beyond the quasistatic approximation. *Phys Rev B* 62:11230
20. Xu H, Aizpurua J, Apell SP, Käll M (2000) Electromagnetic contributions to single-molecule sensitivity in Surface-enhanced Raman scattering. *Phys Rev E* 62:4318
21. Dvoynenko MM, Goncharenko AV, Romaniuk VR, Venger EF (2001) Effects of dimension on optical transmittance of semicontinuous gold. *Physica B* 299:88
22. Raether H (1988) *Surface Plasmons on Smooth and Rough Surfaces and on Gratings* (Springer Tracts in Modern Physics, Vol. 111), Springer-Verlag, Berlin
23. Wokaun AW (1984) Surface enhanced electromagnetic processes. *Solid State Phys* 38:223
24. Lynch DW, Hunter WR (1985) In: Palik ED (Ed) *Handbook of Optical Constants of Solids*. Academic Press, San Diego, pp 275
25. Crozier KB, Sundaramurthy A, Kino GS, Quate CF (2003) Optical antennas: Resonators for local field enhancement. *J Appl Phys* 94:4632
26. Ruck TG (1970) *Radar Cross Section Handbook*. Plenum press, New York
27. Kreibig U and Vollmer M (1995) *Optical Properties of Metal Clusters*. Springer, Berlin/Heidelberg
28. Martin YC, Hamann HF, Wickramasinghe HK (2001) Strength of the electric field in apertureless near-field optical microscopy. *J Appl Phys* 89:5774
29. Neubrech F, Kolb T, Lovrincic R, Fahsold G, Aizpurua J, Toimil-Molares ME, Karim S, Cornelius TW, Neumann R, and Pucci A (2006) Resonances of individual metal nanowires in the infrared. *Appl Phys Lett* 89:253104
30. Link S, Mohamed MB, El-Sayed MA (1999b) Simulation of the optical absorption spectra of gold nanorods as a function of their aspect ratio and the effect of the medium dielectric constant. *J Phys Chem B* 103:3073
31. Billot L, Lamy de la Chapelle A, Grimault AS, Vial A, Barchiesi D, Bijeon JL, Adam PM, Royer P (2006) Surface enhanced raman scattering on gold nanowire arrays: evidence of strong multipolar surface plasmon resonance enhancement. *Chem Phys Lett* 422:303
32. Imura K, Nagahara T, Okamoto H (2004) Coacervate formation from natural glycolipid: One acetyl group on the headgroup triggers coacervate-to-vesicle transition. *J Am Chem Soc* 126:12730
33. Imura K, Nagahara T, Okamoto H (2005a) Near-field two-photon-induced photoluminescence from single gold nanorods and imaging of plasmon modes. *J Phys Chem B* 109:13214

34. Imura K, Nagahara T, Okamoto H (2005b) Near-field optical imaging of plasmon modes in gold nanorods. *J Chem Phys* 122:154701
35. Grand J, Adam PM, Grimault AS, Vial A, Lamy de la Chapelle M, Bijeon JL, Kostcheev S, Royer P (2006) Optical extinction spectroscopy of oblate, prolate, and ellipsoid shaped gold nanoparticles: Experiments and theory. *Plasmonics* 1:135
36. Little JW, Callcott TA, Ferrell TL, Arakawa ET (1984) Surface-plasmon radiation from ellipsoidal silver spheroids. *Phys Rev B* 29:1606
37. Purcell EM and Pennypacker CR (1973) Scattering and absorption of light by non-spherical dielectric grains. *Astrophys J* 186:705
38. Miller EK (1994) Time domain modelling in electromagnetics. *J Electromagn Waves Appl* 8:1125–72
39. Hafner Ch, Ballist R (1983) The multiple multipole method (MMP). *Int J Comput Electr Electron Eng* 2:1
40. Pendry JB and MacKinnon A (1992) Calculation of photon dispersion relations. *Phys Rev Lett* 69:2772
41. García de Abajo FJ, Howie A (1998) Relativistic electron energy loss and electron induced photon emission in inhomogeneous dielectrics. *Phys Rev Lett* 80: 5180
42. García de Abajo FJ, Howie A (2002) Retarded field calculation of electron energy loss in inhomogeneous dielectrics. *Phys Rev B* 75:115418
43. Aizpurua J, Hanarp P, Sutherland D, Bryant GW, Garcia de Abajo FJ, Kall M (2003) Optical properties of nanorings. *Phys Rev Lett* 90:057401
44. Bryant GW, García de Abajo FJ, and Aizpurua J (2008) Mapping the plasmon resonances of metallic nanoantennas. *Nano Lett* 8: 631
45. Hillenbrand R, Taubner, Keilmann F (2002) Phonon-enhanced light–matter interaction at the nanometer scale. *Nature* 418:159
46. Hu J, Li L, Yang W, Manna L, Wang L, Alivisatos AP (2001) Linearly polarized Emission from colloidal semiconductor quantum rods. *Science* 292:2060
47. Gómez Rivas J, Kuttge M, Kurz H, Haring Bolivar P, Sánchez-Gil JA (2006) Low-frequency active surface plasmon optics on semiconductors. *Appl Phys Lett* 88:082106, 1
48. Englebienne P (1998) Use of colloidal gold surface plasmon resonance peak shift to infer affinity constants from the interactions between protein antigens and antibodies specific for single or multiple epitopes. *Analyst* 123:1599
49. McFarland AD, Van Duyne RP (2003) Single silver nanoparticles as real-time optical sensors with zeptomole sensitivity. *Nano Lett* 3:1057
50. Raschke G, Kowarik S, Franzl T, Soennichsen C, Klar TA, et al. (2003). Biomolecular recognition based on single gold nanoparticle light scattering. *Nano Lett* 3:935
51. Liebsch A and Persson BNJ (1983) Optical properties of small metallic particles in a continuous dielectric medium. *J Phys C* 16:5375
52. Prodan E, Radloff C, Halas NJ, Nordlander P (2003) A hybridization model for the plasmon response of complex nanostructures. *Science* 302:419
53. Emory SR, Nie S (1997) Probing single molecules and single nanoparticles by surface-enhanced Raman scattering. *Science* 275:1102
54. Kneipp K, Wang Y, Kneipp H, Perelman LT, Itzkan I, et al. (1997) Single molecule detection using surface-enhanced Raman scattering (SERS). *Phys Rev Lett* 78:1667
55. Xu H, Bjerneld EJ, Käll M, Börjesson L (1999) Spectroscopy of single hemoglobin molecules by surface enhanced Raman scattering. *Phys Rev Lett* 83:4357
56. Romero I, Aizpurua J, Bryant GW, García de Abajo FJ (2006) Plasmons in nearly touching metallic nanoparticles: Singular response in the limit of touching dimers. *Optics Express* 14:9988
57. Fromm DP, Sundaramurthy A, Schuck J, Kino G, Moerner WE (2004) Gap-dependent optical coupling of single “bowtie” nanoantennas resonant in the visible. *Nano Lett* 4:957
58. Li K, Stockman MI, Bergman DJ (2003) Self-similar chain of metal nanospheres as an efficient nanolens. *Phys Rev Lett* 91, 227402
59. Hao E, Schatz G (2004) Electromagnetic fields around silver nanoparticles and dimers. *J Chem Phys* 120:357

60. Mühlischlegel P, Eisler HJ, Martin OJF, Hecht B, Pohl DW (2005) Resonant optical antennas. *Science* 308:1607
61. Karim S, Toimil-Molares ME, Maurer F, Miehe G, Ensinger W, Liu J, Cornelius TW, Neumann R (2006a) Synthesis of gold nanowires with controlled crystallographic characteristics. *Appl Phys A* 84:403
62. Karim S, Toimil-Molares ME, Balogh AG, Ensinger W, Cornelius TW, Khan EU, and Neumann R (2006b) Morphological evolution of Au nanowires controlled by Rayleigh instability. *Nanotechnology* 17:5954
63. Liu J, Duan JL, Toimil-Molares ME, Karim S, Cornelius TW, Dobrev D, Yao HJ, Sun YM, Hou MD, Mo D, Wang ZG, and Neumann R (2006) Electrochemical fabrication of single crystalline and polycrystalline Au nanowires: the influence of deposition parameters. *Nanotechnology* 17:1922
64. Toimil Molares EM, Brötz J, Buschmann, Dobrev D, Neumann R, Scholz R, Schuchert IU, Trautmann C, and Vetter J (2001a) Etched heavy ion tracks in polycarbonate as templates for copper nanowires. *Nucl Instr Meth B* 185:192
65. Toimil Molares ME, Buschmann V, Dobrev D, Neumann R, Scholz R, Schuchert IU, and Vetter J (2001b) Single-crystalline copper nanowires produced by electrochemical deposition in polymeric ion track membranes. *Adv Mat* 13:62
66. Cornelius TW, Brötz J, Chtanko N, Dobrev D, Miehe G, Neumann R, Toimil Molares ME (2005) Controlled fabrication of poly- and single-crystalline bismuth nanowires. *Nanotechnology* 16:246
67. Cornelius TW, Toimil-Molares ME, Neumann R, Karim S (2006) Finite-size effects in the electrical transport properties of single bismuth nanowires. *J Appl Phys* 100:114307
68. Toimil Molares ME, Höhberger EM, Schaefflein C, Blick RH, Neumann R, and Trautmann C (2003) Electrical characterization of electrochemically grown single copper nanowires. *Appl Phys Lett* 8:2139
69. Toimil-Molares ME, Balogh AG, Cornelius TW, Trautmann C, and Neumann R (2004) Fragmentation of nanowires driven by Rayleigh instability. *Appl Phys Lett* 85:5337
70. Rayleigh L (1878) On the instability of jets. *Proc Lond Math Soc* 10:4
71. Nichols FA, and Mullins WW (1965) Surface- (Interface-) and Volume-diffusion contributions to morphological changes driven by capillarity. *Trans Metal Soc AIME* 233:1840
72. Laurent G, Félidj N, Aubard J, Lévi G, Krenn JR, Hohenau A, Schider G, Leitner A, and Aussenegg FR (2005a) Evidence of multipolar excitations in surface enhanced Raman scattering. *Phys Rev B* 71:045430
73. Laurent G, Félidj N, Aubard J, Lévi G, Krenn JR, Hohenau A, Schider G, Leitner A, Aussenegg FR (2005b) Surface enhanced Raman scattering arising from multipolar plasmon excitation. *J Chem Phys* 122: 011102
74. Teschner U and Huebner K (1990) IR-spectroscopic data of thin insulating films on semiconductors. New methods of interpretation and analysis. *Phys Status Solidi B* 159:917
75. Berreman DW (1963) Infrared absorption at longitudinal optic frequency. *Cubic Cryst Films Phys Rev* 130:2193
76. Fumeaux C, Gritz MA, Codreanu I, Schaich WL, Gonzalez FJ, Boreman GD 2000 Measurement of the resonant lengths of infrared dipole antennas. *Infrared PhysTech* 41:271
77. Ueno K, Mizeikis V, Juodkazis S, Sasaki K, Misawa H (2005) Optical properties of nano-engineered gold block. *Opt Lett* 30:2158
78. Royer P, Bijeon JL, Goudonnet JP, Inagaki T, and Arakawa ET (1989) Optical absorbance of silver oblate particles substrate and shape effects. *Surface Science* 217:384
79. Krenn JR, Schider G, Rechberger W, Lamprecht B, Leitner A, and Aussenegg FR (2000) Design of multipolar plasmon excitations in silver nanoparticles. *Appl Phys Lett* 77:3379
80. Félidj N, Laurent G, Grand J, Aubard J, Lévi G, Hohenau A, Aussenegg FR, Krenn JR (2006) Far-field Raman imaging of short-wavelength particle plasmons on gold nanorods. *Plasmonics* 1:39
81. Ditlbacher H, Hohenau A, Wagner D, Kreibitz U, Rogers M, Hofer F, Aussenegg FR, Krenn JR (2005) Silver Nanowires as Surface Plasmon Resonators. *Phys Rev Lett* 95:257403

82. Schider G, Krenn JR, Gotschy W, Lamprecht B, Ditlbacher H, Leitner A, and Aussenegg FR (2001) Optical properties of Ag and Au nanowire gratings. *J Appl Phys* 90:3825
83. Nie S, Emory SR (1997) Probing single molecules and single nanoparticles by surface-enhanced Raman scattering. *Science* 275:1102
84. Jeanmarie DL, Duynes RPV (1977) Surface Raman spectroelectrochemistry. *J Electroanal Chem* 84:1
85. Moskovits M (1985) Surface-enhanced spectroscopy. *Rev Mod Phys* 57:783
86. Otto A (2005) The chemical (electronic) contribution to surface-enhanced Raman scattering. *J Raman Spectrosc* 36:497
87. Haynes CL, Duynes RPV. (2003) Plasmon-sampled surface-enhanced Raman excitation spectroscopy. *J Phys Chem B* 107:7426
88. Otto A (1983) On the first layer enhancement in Raman scattering of pyrioline on silver. *J. de Physique C* 10:37
89. Hein M, Dumas P, Sinther M, Priebe A, Lilie P, Bruckbauer A, Pucci A, Otto A (2006) Relation between surface resistance, infrared-, surface enhanced infrared- and surface enhanced Raman-spectroscopy's of C²H⁴ and CO on copper. *Surface Science* 600:1017
90. Lombardi JR, Birke RL, Sanchez LA, Bernard I, and Sun SC (1984) The effect of molecular structure on voltage induced shifts of charge transfer excitation in surface enhanced Raman scattering. *Chem Phys Lett* 104:240
91. Johansson P, Xu H, Käll M (2005) Surface-enhanced Raman scattering and fluorescence near metal particles. *Phys Rev B* 72:035427
92. Xu H, Wang X, Persson MP, Xu HQ, Käll M, Johansson P (2004) Unified treatment of fluorescence and Raman scattering processes near metal surfaces. *Phys Rev Lett* 93:243002
93. Skibbe O, Binder M, Pucci A, Otto A, Electronic contributions to infrared spectra of adsorbate molecules on metal surfaces: ethylene on Cu(111). Submitted to *The Journal of Chemical Physics*
94. Féridj N, Aubard J, Lévi G, Krenn JR, Hohenau A, Schider G, Leitner A, Aussenegg FR (2003) Optimized surface-enhanced Raman scattering on gold nanoparticle arrays. *Appl Phys Lett* 82:3095
95. Grand J, Kostchev S, Bijeon JL, Lamy de la Chapelle M, Adam PM, Rumyantseva A, Le'ronde G, Royer P (2003) Optimization of SERS-active substrates for near-field Raman spectroscopy. *Synth Met* 139:621
96. McFarland AD, Young MA, Dieringer JA, and Van Duynes RP (2005) Wavelength-scanned surface-enhanced Raman excitation spectroscopy. *J Phys Chem B* 109:11279
97. Wang H, Levin CS, Halas NJ (2005) Nanosphere arrays with controlled sub-10 nm gap as surface-enhanced Raman spectroscopy substrates. *J Am Chem Soc* 127:14992
98. Débarre A, Jaffiol R, Julien C, Nutarelli D, Richard A, Tchénio P, Chaput F, Boilot JP (2004) Quantitative determination of the 3D dipole orientation of single molecules. *Eur Phys J D* 28: 67
99. Novotny L, Sanchez EJ, Xie XS (1998) Near-field optical imaging using metal tips illuminated by higher-order Hermite–Gaussian beams. *Ultramicroscopy* 71:21
100. Yang W, Hulteen J, Schatz GC, and Duynes RV (1996) A surface-enhanced hyper-Raman and surface-enhanced Raman scattering study of trans-1,2-bis(4-pyridyl)ethylene adsorbed onto silver film over nanosphere electrodes. Vibrational assignments: Experiment and theory. *J Chem Phys* 104 4313
101. Grimault AS, Vial A, Lamy de la Chapelle M (2006) Modeling of regular gold nanostructures arrays for SERS applications using a 3D FDTD method. *Appl Phys B* 84:115
102. Vial A, Grimault AS, Macias D, Barchiesi D, Lamy de la Chapelle M (2005) Improved analytical fit of gold dispersion: Application to the modeling of extinction spectra with a finite-difference time-domain method. *Phys Rev B* 71:085416
103. Calander N, Willander M (2002) Theory of surface-plasmon resonance optical field enhancement at prolate spheroids. *J Appl Phys* 92: 4878
104. Hartstein A, Kirtley JR, Tsang JC. (1980) Enhancement of the Infrared absorption from molecular monolayers with thin metal overlayers. *Phys Rev Lett* 45:201

105. Aroca RF, Ross DJ, Domingo C (2004) Surface-Enhanced Infrared Spectroscopy. *Appl Spectrosc* 58: 324A
106. Enders D, Pucci A (2006) Surface enhanced infrared absorption of octadecanethiol on wet chemically prepared Au nanoparticle films. *Appl Phys Lett* 88:184104
107. Osawa M (2001) Near-Field Optics and Surface Plasmon Polaritons. in: *Topics in Applied Physics*, Vol. 81, Springer, Berlin/Heidelberg, p 163
108. Priebe A, Pucci A, and Otto A (2006) Infrared reflection-absorption spectra of C₂H₄ and C₂H₆ on Cu: Effect of surface roughness. *J Phys Chem B* 110:1673
109. Priebe A, Sinther M, Fahsold G, and Pucci A (2003) The correlation between film thickness and adsorbate line shape in surface enhanced infrared absorption. *J Chem Phys* 119:4887
110. Priebe A, Fahsold G, and Pucci A (2004) Strong pyramidal growth of metal films studied with IR transmittance and SEIRA of CO. *J Phys Chem B* 108:18174
111. Bjerke AE, Griffiths PR, Theiss W (1999) Surface-enhanced infrared absorption of CO on platinumized platinum. *Anal Chem* 71:1967
112. Ducourtieux S, Podolskiy VA, Grésillon S, Buil S, Berini B, Gadenne P, Boccara AC, Rivoal JC, Bragg WD, Banerjee K, Safonov VP, Drachev VP, Ying ZC, Sarychev AK, Shalaev VM (2001) Near-Field Optical Studies of Semicontinuous Metal Films. *Phys Rev B* 64:165403
113. Pucci A (2005) IR spectroscopy of adsorbates on ultrathin metal films: Advanced optical diagnostics of surfaces, nanostructures, and ultrathin films. *Physica Status Solidi (b)* 242:2704
114. Schreiber F (2000) Structure and growth of self-assembling monolayers. *Prog Surf Sci* 65:151
115. Seo EK et al. (2004) Atomic layer deposition of titanium oxide on self-assembled-monolayer coated gold. *Chem Mater* 16:1878
116. Lin-Vien D, Colthup NB, Fateley WG, and Grasselli JG (1991) *The Handbook of Infrared and Raman Characteristic Frequencies of Organic Molecules*. Academic Press, San Diego, pp. 9
117. Neubrech F, Pucci A, Cornelius TW, Karim S, García-Etxarri A, and Aizpurua J (2008) Resonant plasmonic and vibrational coupling in a tailored nanoantenna for infrared detection. Submitted to *Phys Rev Lett*
118. Bouhelier A, Bachelot R, Lerondel G, Kostcheev S, Royer S, Wiederrecht G (2005) Surface plasmon characteristics of tunable photoluminescence in single gold nanorods. *Phys Rev Lett*. 95:267405
119. Taminiau TH, Moerland RJ, Segerink FB, Kuipers L, van NF (2007) $\lambda/4$ Resonance of an optical monopole antenna probed by single molecule fluorescence. *Nano Lett* 7:28